Simultaneous Positioning and Communications:

Hybrid Radio Architecture, Estimation Techniques, and Experimental Validation

by

Andrew Herschfelt

A Dissertation Presented in Partial Fulfillment
of the Requirement for the Degree
Doctor of Philosophy

Approved October 2019 by the
Graduate Supervisory Committee:

Daniel W. Bliss, Chair
Douglas Cochran
Christ Richmond
Ahmed Alkhateeb

ARIZONA STATE UNIVERSITY

December 2019

ABSTRACT

Limited spectral access motivates technologies that adapt to diminishing resources and increasingly cluttered environments. A joint positioning-communications system is designed and implemented on consumer-off-the-shelf (COTS) hardware. This system enables simultaneous positioning of, and communications between, nodes in a distributed network of base-stations and unmanned aerial systems (UASs). This technology offers extreme ranging precision (< 5 cm) with minimal bandwidth (10 MHz), a secure communications link to protect against cyberattacks, a small form factor that enables integration into numerous platforms, and minimal resource consumption which supports high-density networks. The positioning and communications tasks are performed simultaneously with a single, co-use waveform, which efficiently utilizes limited resources and supports higher user densities. The positioning task uses a cooperative, point-to-point synchronization protocol to estimate the relative position and orientation of all users within the network. The communications task distributes positioning information between users and secures the positioning task against cyberattacks. This high-performance system is enabled by advanced time-of-arrival estimation techniques and a modern phase-accurate distributed coherence synchronization algorithm. This technology may be installed in ground-stations, ground vehicles, unmanned aerial systems, and airborne vehicles, enabling a highly-mobile, re-configurable network with numerous applications.

ACKNOWLEDGMENTS

I would like to express my gratitude to the following individuals for their time and effort: my advisor, Dr. Daniel Bliss, for his guidance, patience, and wisdom; my parents, Paul Herschfelt and Kelly Everill, for their continued support and encouragement; and my advisory committee, Dr. Douglas Cochran, Dr. Christ Richmond, and Dr. Ahmed Alkhateeb, for their time and feedback. I would also like to thank my colleagues and co-authors for their contributions to this body of work, including Sharanya Srinivas, Hanguang Yu, Shunyao Wu, Yang Li, Hyunseok Lee, Owen Ma, Brittany McCall, Dr. Chaitali Chakrabarti, Dr. Alex Chiriyath, Dr. Yu Rong, Dr. Richard Gutierrez, Dr. Constantine Balanis, and Dr. Craig Birtcher. I am further grateful to my academic advisors Lynn Pratte and Toni Mengert for their advice and guidance. Finally, I would like to thank my partner Victoria Flys for her continued support.

This body of research was funded by Airbus through the Hyper-Precise Positioning and Communications (HPPC) program. Thank you to Nunzio Sciammetta, Klaus Rueger, Bruno Pasquier, and the entire Airbus team for making this possible.

TABLE OF CONTENTS

LIST OF TABLES

LIST OF FIGURES

Figure Page

Figure Page

LIST OF ABBREVIATIONS

ADS-B	Automatic Dependent Surveillance - Broadcast
AoA	Angle-of-Arrival
APNT	Alternative Positioning, Navigation, and Timing
ATM	Air Traffic Management
AWGN	Additive White Gaussian Noise
CCAWGN	Circularly-Symmetric AWGN
CE-OFDM	Constant Envelope OFDM
CFO	Carrier Frequency Offset
COTS	Consumer off the Shelf
CPM	Continuous Phase Modulation
CRLB	Cramér-Rao Lower Bound
CSS	Chirp Spread Spectrum
DLL	Data Link Layer
DME	Distance Measuring Equipment
DSSS	Direct Sequence Spread Spectrum
FDD	Frequency Division Duplexing
GDOP	Geometric Dilution of Precision
GNSS	Global Navigation Satellite System
GPS	Global Positioning System
ITS	Intelligent Transport System(s)

JPC	Joint Positioning-Communications
LDACS1	L-Band Digital Aeronautical Comm. System 1
LFM	Linear Frequency Modulation
LiDAR	Light Detection and Ranging
Li-Fi	Light-Fidelity
LTE	Long-Term Evolution
NTP	Network Timing Protocol
OFDM	Orthogonal Frequency-Division Multiplexing
OSI	Open Systems Interconnect
PAPR	Peak-to-Average Power Ratio
PCFM	Polyphase-Coded Frequency Modulation
PL	Pseudo-Lite
PNT	Positioning, Navigation, and Timing
P-WAM	Passive Wide Area Multilateration
RF	Radio Frequency
RFID	Radio Frequency Identification
RMS	Root Mean Square
RToF	Roundtrip Time-of-Flight
SDR	Software-Defined Radio(s)
SISO	Single-Input Single-Output
SNR	Signal to Noise Ratio
SWAP	Size, Weight, and Power
TDD	Time Division Duplexing

TDOA	Time Difference of Arrival
ToA	Time-of-Arrival
ToF	Time-of-Flight
UAS	Unmanned Aerial System(s)
UAV	Unmanned Aerial Vehicles(s)
V2V	Vehicle to Vehicle
VHF	Very High Frequency
VOR	VHF Omnidirectional Range

Chapter 1

INTRODUCTION

Limited spectral access motivates technologies that adapt to diminishing resources and increasingly cluttered environments. Modern radio applications demand better performance, with fewer resources and at higher user densities, than legacy systems can support. In this study, we address these demands in the context of vehicular communications, positioning, navigation, and timing. We design and implement a dual-function radio system that simultaneously performs positioning and communications tasks, which enable numerous applications. This system is resource efficient, enabling higher user densities within existing allocations, while simultaneously executing high-precision positioning, timing synchronization, and distributed communications with less power, bandwidth, and infrastructure than similar technologies.

This technology has numerous applications to modern vehicle systems. High-precision relative positioning enables applications such as collision avoidance, automated landing, navigation, and formation control. Secure network communications enable distributed knowledge base, real-time traffic conditions, and air traffic management, and when combined with the positioning task maintains distributed coherence between users. The system flexibility allows quick and easy installation in areas without existing coverage, providing immediate support in situations such as disaster relief or forward operating bases. This technology further supports automation of vehicular transport by providing a cooperative medium between users, enabling vehicle-to-vehicle communications and remote control.

This study exploits numerous modern innovations in the fields of software-defined radio (SDR), electromagnetic radio frequency (RF) convergence, and distributed coherence. Modern co-use waveform design techniques enable simultaneous execution of both the communications and positioning tasks. Novel time-of-arrival (ToA) estimation techniques and time-of-flight (ToF) synchronization algorithms enable high-precision position and orientation estimation. Modern COTS SDRs allow low-cost implementation on a variety of physical platforms. These innovations culminate in a novel approach to traditional problems that addresses the limitations of legacy systems in modern environments.

The following chapters discuss the technical basis and capabilities of this novel system. In this chapter, I discuss the primary functions of this system and its place in the context of modern vehicular radio systems. I further review existing literature in a variety of relevant fields. In Chapter 2, I present the basic system architecture. In Chapter 3, I define time and propagation models for the following estimation techniques. In Chapter 4, I discuss novel ToA estimators and compare a range of estimation techniques using Monte Carlo simulations. In Chapter 5, I discuss the ToF estimation and time-synchronization algorithm. In Chapter 6, I address many of the technical considerations made during the design and implementation of the system. In Chapter 7, I present experimental results as validation of the proposed system. In Chapter 8, I summarize the current state of the system and propose avenues of future research.

1.1 System Overview

The joint positioning-communications system is a hybrid RF system that simultaneously performs positioning and communications tasks. This system specifically addresses the issue of spectral congestion by employing an extremely efficient positioning strategy and using a co-use waveform that simultaneously performs both tasks. This efficiency in turn supports more users in a given frequency allocation. These tasks support a synchronization algorithm that enables a distributed-coherence task, which synchronizes the clocks of all connected users.

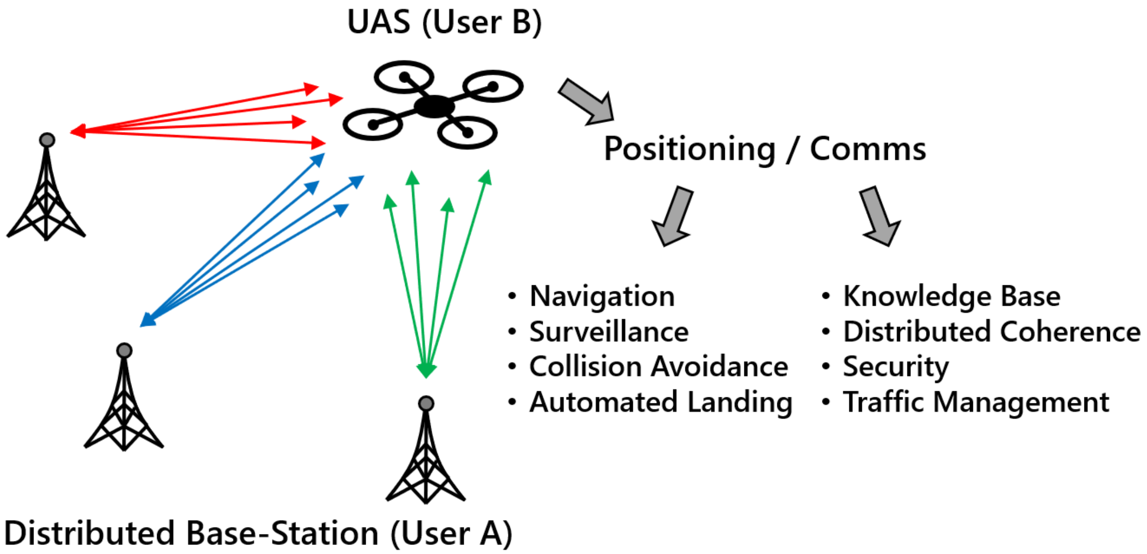

Figure 1.1: Example 3x4 system configuration with a 4-antenna UAS and a 3-antenna distributed base-station. This configuration forms 12 links between the users, over which the communications payloads and positioning sequences are transmitted. Each user independently estimates the lengths of each link with a ToF estimation algorithm.

The positioning task is performed using advanced ToA estimation techniques and a synchronization algorithm that measures ToF between all pairs of antennas between two users. These users alternate transmitting and receiving the co-use waveform, which contains timing information and positioning reference sequences. An example configuration with a base-station and unmanned aerial system (UAS) is depicted in Figure 2.4. Multi-antenna radio platforms provide spatial diversity which can be used to estimate relative position and orientation. This system operates with 10 MHz bandwidth and maintains a ranging standard deviation below 5 cm for up to 2 km of range. In controlled configurations, this deviation can be driven as low as 1 mm.

1.1.1 Novelty

This system's capabilities are enabled by numerous novel innovations. This includes:

1. Co-use waveform and receiver design: This system operates using a joint positioning-communications waveform that combines both tasks into a single waveform. This mitigates mutual interference between the two and enables high-resource efficiency. This further allows each task to be tuned simultaneously because both tasks are controlled by a single processing chain.

2. Phase-accurate ToA estimation: The distances between antennas are estimated by finding the difference between transmit and receive timestamps. The transmit timestamps are shared in the communications payload, but the received timestamp must be estimated. A phase-accurate ToA estimator is designed and implemented to produce phase-accurate estimates of the received timestamps. This enables high-precision distance estimates with minimal spectral resources. This concept has been demonstrated in previous publications [1, 2] and is extended here to a complete positioning system.

3. ToF synchronization algorithm: This system utilizes a novel algorithm that simultaneously estimates the ToF between all antenna pairs and synchronizes the clocks of the interacting users. This algorithm precisely estimates and tracks the

differences between the user clocks and allows them to achieve phase-accurate distributed coherence.

4. Commercial-off-the-shelf (COTS) hardware: This system is implemented on commercially available SDR hardware, making it accessible and low-cost. This limits the necessary infrastructure to implement a working system and reduces the cost and labor of building user platforms.

1.1.2 Advantages and Applications

This technology has numerous advantages over similar legacy systems. The positioning tasks achieves high precision ranging estimates ($\sigma < 5$ cm) with limited bandwidth (10 MHz) and limited acquisition time ($< 2 - 3$ s). The joint waveform efficiently utilizes spectral resources, which supports higher user densities in network configurations and enables more tasks per bandwidth allocation. This system is implemented on COTS hardware, making it accessible, low-cost, and flexible. The small form factor allows installation on a variety of platforms, and the system does not require existing infrastructure, so it can easily be deployed in new environments without existing coverage.

This technology has numerous applications to modern vehicle systems. High-precision relative positioning enables collision avoidance, automated landing, navigation, and formation control. Secure network communications enable distributed knowledge base, real-time traffic conditions, and air traffic management. Combined, both tasks maintain distributed phase-coherence between users. The system flexibility allows quick and easy installation in areas without existing infrastructure, providing immediate coverage in situations such as disaster relief or forward operating bases.

This technology further supports automation of vehicular transport by providing a cooperative medium between users, enabling vehicle-to-vehicle communications and remote control.

1.2 Background

The joint positioning-communciations system is a fusion of several technologies that leverages results from numerous fields of research. The study of such hybrid RF systems was coined "RF Convergence" in [3]. In this work, the authors explore the problem of spectral congestion and survey the existing literature on co-operative techniques between various RF systems. They observe that legacy system design techniques will not satisfy the growing demand for spectral access, but they also demonstrate that modern co-operation and co-design methods can not only mitigate spectral congestion, but also increase individual user performance. The proposed joint positioning-communications system is an example of a co-design technique, in which two systems are designed and implemented jointly. By designing both systems simultaneously, we can better mitigate interference between the two tasks and leverage the joint processing chain to improve the performance of both.

Other relevant fields include joint waveform design, ToA estimation, distributed coherence, and positioning, navigation, and timing (PNT) systems. I briefly discuss some relevant publications in each field to provide context and motivation for this system.

1.2.1 RF Convergence

Spectral congestion limits the capabilities and opportunities of radio systems. Radio-Frequency (RF) Convergence refers to a growing movement of co-operation, co-existence, and co-design techniques that allow modern radio systems to adapt to cluttered environments and exploit their neighbors for mutual benefit [3]. The proposed system is an example of simultaneous sensing and communications, which has numerous applications to modern technologies.

One increasingly popular application of the proposed technology lies in intelligent transport systems (ITS), specifically self driving cars and unmanned aerial vehicles (UAVs). These vehicles need both vehicle-to-vehicle (V2V) communications and navigation systems. Numerous V2V communications technologies already exist [4, 5], and the field continues to evolve as the technologies improve. Many collision avoidance technologies have also been considered, including radar systems for ground vehicles [6, 7] and UAVs [8, 9], light-fidelity (Li-Fi) systems [10, 11], and Lidar systems [12–14]. Other related applications include air traffic management (ATM) and flight control [15–17], and asset tracking [18, 19], which again require a communications medium and a positioning system.

The proposed joint positioning-communications system enables these applications with a single radio platform by providing both the communications and positioning tasks necessary to implement them. By consolidating both tasks into a single system, we reduce the amount of necessary hardware, limit the power and bandwidth consumption, reduce the complexity of the processing chain, and limit interactions and interference between the two tasks. For unmanned aerial vehicle (UAV) platforms that are especially sensitive to size, weight, and power (SWAP) restrictions, the proposed technology may enable these applications on platforms which are otherwise unable to carry multiple radio systems. For platforms with multiple antennas, the positioning task further outperforms standard radar systems by estimating the orientation of nearby users, enabling even more sensitive applications such as formation control and automated landing.

1.2.2 Joint Waveform Design

One co-design technique for performing multiple tasks simultaneously is to design a joint waveform that contains all the necessary elements for each task. This approach is historically uncommon because the optimal waveforms for different tasks are often extremely different and considered incompatible. As RF hardware improves, however, many of the limitations that drove historical waveform design no longer apply, which affords us more freedom to optimize waveforms for multiple tasks simultaneously. In the context of simultaneous radar and communications, joint waveforms may be broadly characterized as parasitic radar or embedded communications.

Parasitic radar refers to communications waveforms that have been treated to possess suitable radar performance characteristics, such as direct sequence spread spectrum (DSSS) [20–22] and orthogonal frequency-division multiplexing (OFDM). OFDM is commonly used in communications applications, is robust against multipath fading, and may easily be synchronized and equalized [23, 24]. OFDM waveforms also have high peak-to-average power ratio (PAPR) [25], which are difficult to amplify with power efficient amplifiers [26]. Some strategies allocate some subcarriers to communications and some to radar, which allows flexibility in the waveform shape and may reduce PAPR [27]. Constant envelope OFDM (CE-OFDM) addresses the PAPR by modulating the OFDM waveform onto the phase of a constant envelope carrier. This reduces the PAPR to 0 dB but introduces a FM threshold, which makes low SNR operation difficult, and has lower detection performance for a given spectral efficiency. It is also more difficult to extend the modulation scheme to MIMO systems [28, 29]. The cyclic prefix requirement also creates periodic range ambiguities which may adversely affect radar performance [30]. Design requirements for radar and communications using OFDM waveforms are often antipodal, so parameter space selection is motivated by context [31]. Embedded communications refers to embedding communications data into a radar waveform. One common example is chirped spread spectrum (CSS), which encodes data in the phase of linear frequency modulated (LFM) chirp waveforms [32–35]. Other techniques include polyphase-coded frequency modulation (PCFM) [36, 37], continuous phase modulation (CPM) [38], and FM noise radar waveforms [39].

Joint waveform design is extremely dependent on the type of system, the combination of desired tasks, and the necessary performance metrics. To implement the positioning task, we chose a ToA based approach instead of a traditional radar approach. While ToA positioning promises comparable performance at much lower power and bandwidth, this limits the scope to cooperative targets and requires extremely precise timing synchronization. Due to the hybrid nature of the system, the communications task may be leveraged to implement a timing synchronization algorithm, enabling high performance positioning with minimal resources. The joint waveform consists of a communications payload, which contains both arbitrary communications and reserved communications for the positioning task, and positioning reference sequences, which drive a ToA positioning estimation algorithm. The current waveform is single-carrier, which significantly simplifies the processing chain, but lacks the optimization flexibility of a multi-carrier waveform such as OFDM.

1.2.3 Time-of-Arrival Estimation

Time-of-arrival estimation refers to estimating at what time a signal is received. This is limited by how well the transmitter and receiver are synchronized. Several estimators are formulated and compared in [1] and [2] in the context of ranging and clock synchronization. Using ToF estimates has previously been considered for implementing location and ranging systems [40, 41], and has recently become accessible as a low-cost localization solution [42].

Historically, ToA positioning systems were not viable as high-precision positioning systems without massively expensive supporting infrastructure, the most notable example being the Global Positioning System (GPS) [43]. GPS consists of a global network of satellites that transmit radio sequences towards the ground, which users use to triangulate their position. This system provides massive positioning coverage across the planet at reasonable accuracies, but is extraordinarily expensive, at an initial cost of $12 billion to put the constellation in orbit and about $1 billion per year to maintain [44]. Furthermore, these satellites require extremely precise atomic clocks, which are both too large and too heavy to use on small UAVs. Now that local oscillators and software defined radios (SDRs) are cheaper, lighter, higher quality, and more accessible, ToA positioning systems are much more viable as local alternative PNT systems. GPS is also susceptible to adversarial spoofing attacks, which can falsify a receiver's position estimates [45]. Spoofing attacks can be especially catastrophic in airborne applications. The proposed system implicitly addresses this vulnerability by leveraging the communications task as an authentication method required before producing any positioning estimates.

1.2.4 Distributed Coherence

Distributed coherence refers to synchronizing distributed nodes to form a coherent system. In this context, it specifically refers to aligning the user clocks to achieve high-precision positioning. Many technologies rely on synchronized clocks, and many approaches to achieving this have been developed. One common approach is a cooperative protocol known as the network timing protocol (NTP) [46, 47]. Distributed coherent radio systems rely on various synchronization algorithms [48], but we focus on a variant of the NTP that jointly estimates ToF and synchronizes nodes [1].

1.2.5 Alternative Positioning, Navigation, and Timing Systems

Positioning, navigation, timing, and localization are persistent problems with numerous solutions. The Global Navigation Satellite System (GNSS) is the most ubiquitous PNT service, but for sensitive applications such as aircraft navigation and national security, this system is often considered insufficiently reliable. To improve reliability of service in aviation applications, many alternative positioning, navigation, and timing (APNT) technologies have been considered as fallback or supplementary PNT options. In [49], the authors discuss 5 classifications of APNT technologies: distance measuring equipment (DME), passive wide area multilateration (P-WAM), Pseudolite (PL), VHF omnidirectional range (VOR), and L-band Digital Aeronautical Communication System 1 (LDACS1). These systems are disussed briefly below, and their key characteristics are summarized and compared to the proposed technology in Table 1.1.

DME is a roundtrip time-of-flight (RToF) measurement system in which aircraft interrogate ground stations and use the response to estimate the ToF between the platforms [49]. A network of DME ground stations are leveraged to estimate the position of participating aircraft. Legacy DME systems have limited ranging performance ($\sim$ 300 m), but can support better performance ($<$ 100m) with modern hardware upgrades [50].

P-WAM is a passive multilateration system in which aircraft periodically braodcast signals, which are measured by an array of ground stations. These receivers measure the ToA and pass them to a central processor, which uses the time differences of arrival (TDOAs) to estimate the position of the aricraft. This information is then communicated back to the aircraft [49]. This technique has been considered as a passive positioning technique using existing automatic dependent surveillance – broadcast (ADS-B) communications infrastructure [51–55].

PL consists of ground stations that emulate GPS signals to supplement or replace GNSS service. This mitigates long range path loss and the cost of deploying infrastructure, but the system is more susceptible to multi-path interference and must interact carefully with existing GNSS service to avoid collisions. Because of the intrinsic flexibility of the infrastructure, PL augmentation can mitigate performance loss when GNSS services are limited or unavailable [56].

VOR is an angle-of-arrival (AoA) system that uses two reference signals to estimate the location of aircraft. The first signal is transmitted from an omni-driectional antenna, and the second from a highly-directional rotating antenna. When the main lobe of the second antenna is pointing at an aircraft, the difference in phase can be used to estimate the angle of azimuth. VOR is a legacy technology that is being replaced by higher perfomance systems [49].

LDACS1 is an L-band communications system which may be compatible with integrated navigation functions. This may be achieved by measuring pseudo-range between an aircraft and ground-stations, similar to PL approaches. The data link fromed by the LDACS1 system may be leveraged to communicate the necessary information to execute the navigation task. This offers a reasonable APNT solution, expecially considering the competing DME systems in the same frequency band, but consumes some of the communications resources of the LDACS1 system [57].

The joint positioning-communications system functions as both a close-range and long-range positioning system between vehicles and base stations. Vehicle-to-vehicle (V2V) positioning technologies include radar systems [58], light detection and ranging (LiDAR) [5, 59], optical systems [60, 61], and radio frequency identification (RFID) [18]. The most common positioning system, and the closest analog to our hybrid system, is GPS [62, 63]. The relative performance of the proposed technology is compared to the previously discussed APNT technologies in Table 1.1.

Table 1.1: Performance Comparison of APNT Technologies [49-63]

Label	Tech	Carrier	Bandwidth	Precision	Coverage
DME	RToF	960-1215 MHz	252× 1 MHz	(Legacy) $\sim$ 300 m (Modern) $\sim$ 100 m	50 km (Close) 75 km (Mid) 250 km (Long)
(ADS-B) P-WAM	TDoA	(ADS-B) 1090 MHz 978 MHz	(ADS-B) 50 kHz 1.3 MHz	50-100 m	(ADS-B) 250 km
GPS, PL	Pseudo-Range	1.58 GHz (L1) 1.23 GHz (L2)	1 MHz (Civ) 10 MHz (Mil)	5-100 cm 1-5 cm (PL)	Global
VOR	AoA	108-118 MHz	10 MHz	0.35^o-1.4^o	100-300 km
JPC	Pseudo-Range	915 MHz (US) 783 MHz (EU)	10 MHz	1-5 cm (Raw) 1-5 mm (Phase)	10 km

1.3 Technical Challenges

The joint positioning-communications system achieves high precision positioning with fewer resources, higher reliability, and greater security than comparable systems. To achieve this, numerous technical challenges must be addressed.

1.3.1 Precision

The precision of a traditional ranging system is constrained by the system bandwidth. The target precision for the positioning task is 100 times more precise than this intrinsic resolution. Achieving this precision requires high integrated SNR, carrier-phase-accurate time synchronization, and high-precision ToA estimation. The traditional approach to estimating ToA samples a received signal and correlates against a known reference signal. This correlation is usually performed at the sampling frequency or some small multiple thereof. This approach is limited to the time difference between signal samples, or the inverse of the system bandwidth. For a system bandwidth of 10 MHz, this difference corresponds to 30 m, while the target accuracy is below 1 cm. Clearly, this approach is insufficient for achieving the system goals.

This estimation approach can be dramatically improved by performing this correlation at a much finer resolution and using the phase information to compensate the estimate. Between each signal sample, the carrier waveform oscillates many times. If this correlation is performed at a fine enough resolution, this estimate can be isolated to within a single carrier cycle. In this regime, the phase of this correlation can be used to further improve the estimate; otherwise the phase information is ambiguous across carrier cycles.

1.3.2 Distributed Phase Coherence

To achieve phase-accurate ToA estimates, the clocks on each radio platform must be precisely synchronized. Specifically, this synchronization must be precise to within a fraction of a carrier cycle. The timing exchange synchronization algorithm simultaneously estimates the ToF between all pairs of antennas and several clock parameters to digitally synchronize the clock sources.

1.3.3 Co-Channel Interference

This system operates at low power in a narrow bandwidth, and is therefore sensitive to interference from nearby frequency channels. This co-channel interference may limit the performance capabilities of the system without sufficient mitigation techniques.

1.3.4 Security

Security against adversarial threats restricts and motivates many of our design choices. The primary security threat with which we are concerned is an adversary providing false information to the system with intent to manipulate the flight path of the platform. This will be counteracted by avoiding reliance on less secure systems such as GPS, and instead developing a robust positioning approach. This includes dynamic encryption with dynamic key distribution and time-limited keys, which prevent an adversary from creating false messages that appear legitimate. The simultaneous communications task enables these countermeasures.

1.3.5 Legacy System Interaction

The design process of this technology must also consider the existence of legacy systems operating in the same environments. When possible, a spectral isolation approach may resolve most conflicts. Interference to legacy systems may be reduced by employing power-efficient spread-spectrum links. Interference from narrowband legacy systems may likewise be addressed with various interference mitigation techniques.

Chapter 2

SYSTEM ARCHITECTURE

In this chapter, we discuss the major components of the joint positioning-communications radio architecture. The two major components are the data link layer (DLL), which controls how users interact with each other and access the medium; and the physical layer, which defines how each user generates transmissions and receive data. I additionally discuss key elements of the hybrid processing chain.

2.1 Data Link Layer

The DLL is one of the 7 standard layers in the Open System Interconnect (OSI) radio model [64]. This layer describes how users in a network transfer data, including how that data is packaged and when users are allowed to access the communications medium.

Users interact by alternately transmitting and receiving joint positioning-communications waveforms, which contain information payloads and positioning sequences. Upon receiving a transmission, a given user estimates the time at which the waveform arrived, decodes the communications payload, and packages the collected data, and prepares a packet for transmission. Transmission events are scheduled every 50 ms, with a waveform duration of 10 ms, and a master node controls which users are allowed to transmimt during which events. An example medium access schedule is depicted in Figure 2.1,

A transmission contains a communications segment and a positioning segment. The communications segment contains a data payload and several pilot sequences.

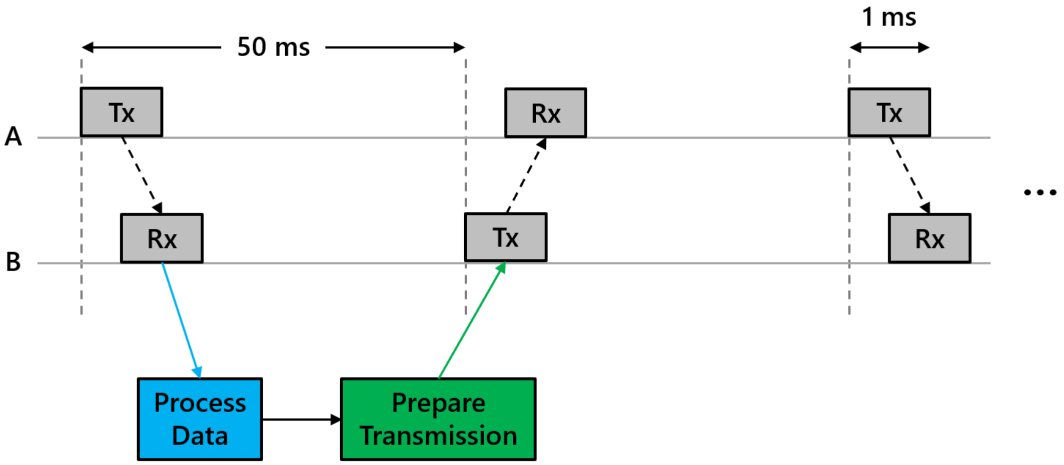

Figure 2.1: Depiction of data link layer for 2 users. Users alternate transmitting and receiving in each frame. The receiver estimates the ToA timestamps and schedules the transmit timestamp, all of which are packaged into the next payload and transmitted during the next frame.

The positioning segment is a time-division duplexed (TDD) series of positioning sequences transmitted from different transmit antennas. Each antenna transmits a short positioning sequence in different time slots as depicted in Figure 2.2. For users with four antennas, 4 positioning sequences are transmitted, all of which are received by each receive antenna, forming 16 links. The receiver estimates the ToA of each sequence on each receive channel.

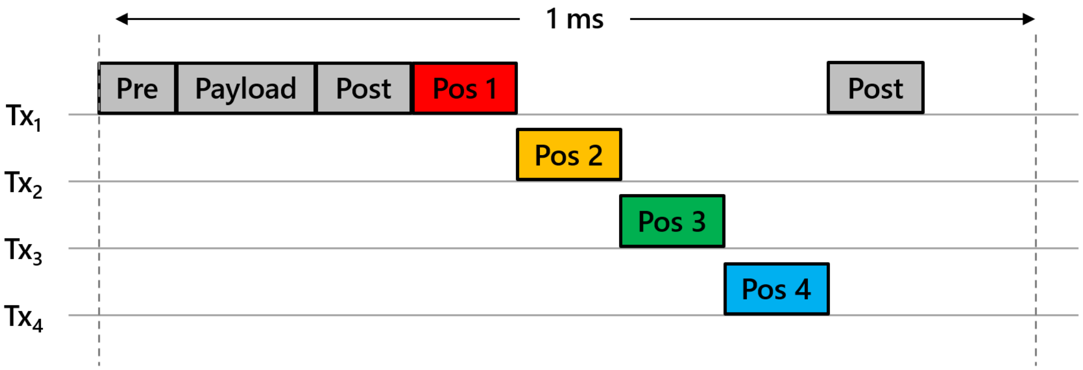

Figure 2.2: Depiction of TDD positioning scheme for a user with 4 antennas. The communications payload is transmitted on antenna one, then each antenna takes turns transmitting a unique positioning sequence. All of these elements together compose the Tx block depicted in Figure 2.1.

2.2 Physical Layer

The physical layer is another standard layer in the OSI stack. This layer refers to the physical waveforms that each user generates and the medium through which they are transmitted. I briefly describe the major aspects of the waveform that each user generates and transmits.

2.2.1 Waveform Structure

I define the individual components of the joint positioning-communications waveform. The complete waveform is depicted in Figure 2.3. The communications segment consists of a preamble, 2 postambles, and a data payload. The preamble and postambles are used to estimate frequency offsets for the communications processing chain. The positioning sequences are transmitted sequentially from the 4 transmit antennas. Empty buffers are placed between each component to mitigate multi-path and inter-symbol interference.

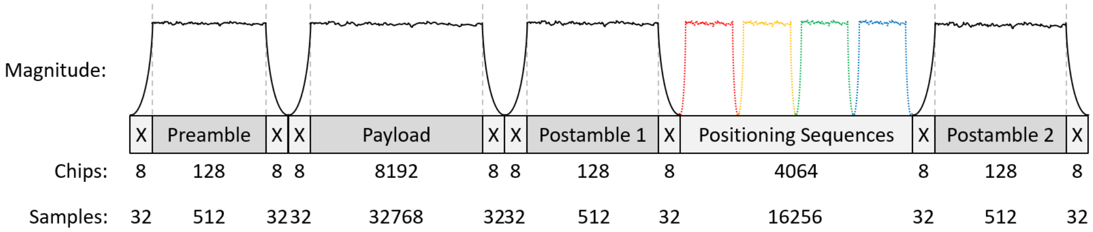

Figure 2.3: Individual components of the joint waveform. The length of each component is defined in number of critical samples, or chips. The communications component consists of a preamble, 2 postambles, and a payload. The positioning sequences are transmitted sequentially by the 4 transmit antennas. Each component is buffered with empty space to mitigate multi-path and inter-symbol interference

2.2.2 Antenna Links

For two multi-antenna users, each antenna on each platform forms a link. The receiving platform estimates the distance between each link. Each system must know how many antennas the other uses, and which positioning sequences are being transmitted from each. They must also know the geometry of the platform to make sense of the distance estimates. This information is shared in the communications payload.

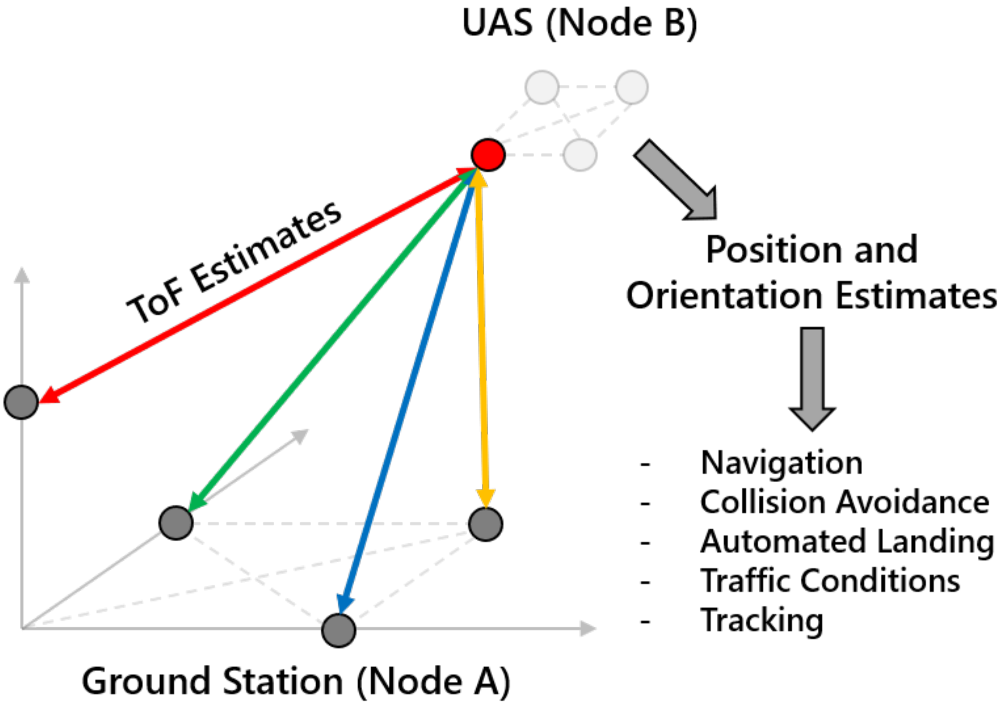

Figure 2.4: Example system configuration with a 4-antenna ground station and 4-antenna UAS. This system forms 16 antenna links. 4 of these links are pictured above while the UAS receives. If the UAS knows the geometry of the base station, these distance estimates and be converted to position and orientation, enabling a variety of applications.

2.3 Processing Chain

Both the positioning and communications tasks are performed simultaneously in a single processing chain. Upon receiving the joint waveform, the receiver decodes the communications payload and estimates the ToA of each positioning sequence on each receive channel. This information is passed to the synchronization algorithm, which estimates the ToF for each antenna link and digitally synchronizes the clock sources. A block diagram of this processing chain is depicted in Figure 2.5.

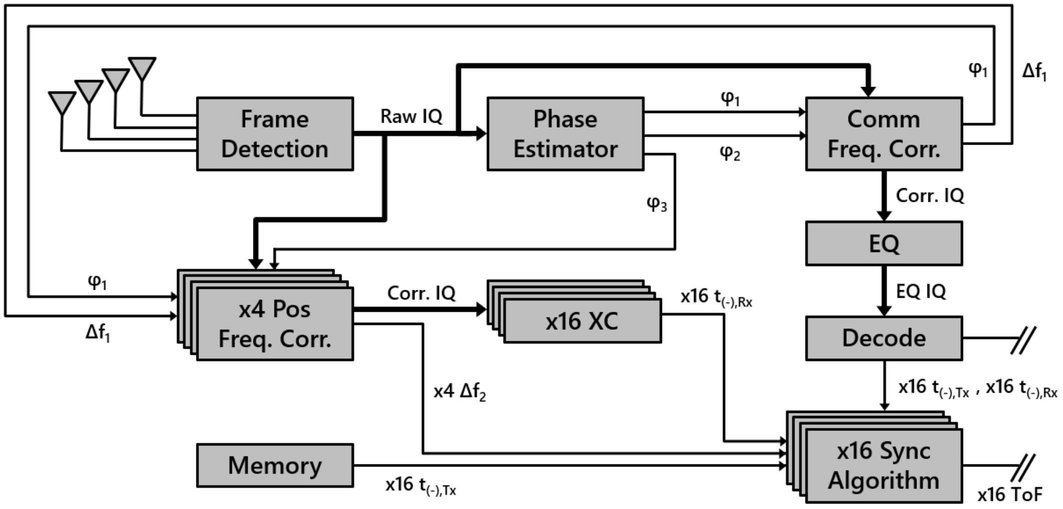

Figure 2.5: Receiver processing chain block diagram. A frame detector collects raw IQ data when the waveform is detected, and passes it to the communications chain (top right) and the positioning chain (bottom left). Frequency corrections are estimated and applied to the raw IQ data. The decoded payload and the 16 ToA estimates are passed to the synchronization algorithm.

2.3.1 Overview

The joint receiver processing chain consists of the following primary functions:

- Frame Detection: Acquires the incoming signals and outputs data vectors to the processing chain.

- Frequency Correction: Estimates and corrects for frequency offsets in the data. Consists of phase estimators, a communications frequency correction, and a positioning frequency correction.
- Equalization: A standard communications equalizer.
- Massive Correlation: Computationally efficient hardware implementation of the ToA estimator.

2.3.2 Frame Detection

The frame detector detects an incoming signal and outputs a data vector to the processing chain. This detector uses the communications preamble to coarsely estimate the time of arrival of transmitter 1 on receive channel 1. The receive buffers for all 4 channels are then output to the processing chain. This is depicted in Figure 2.6.

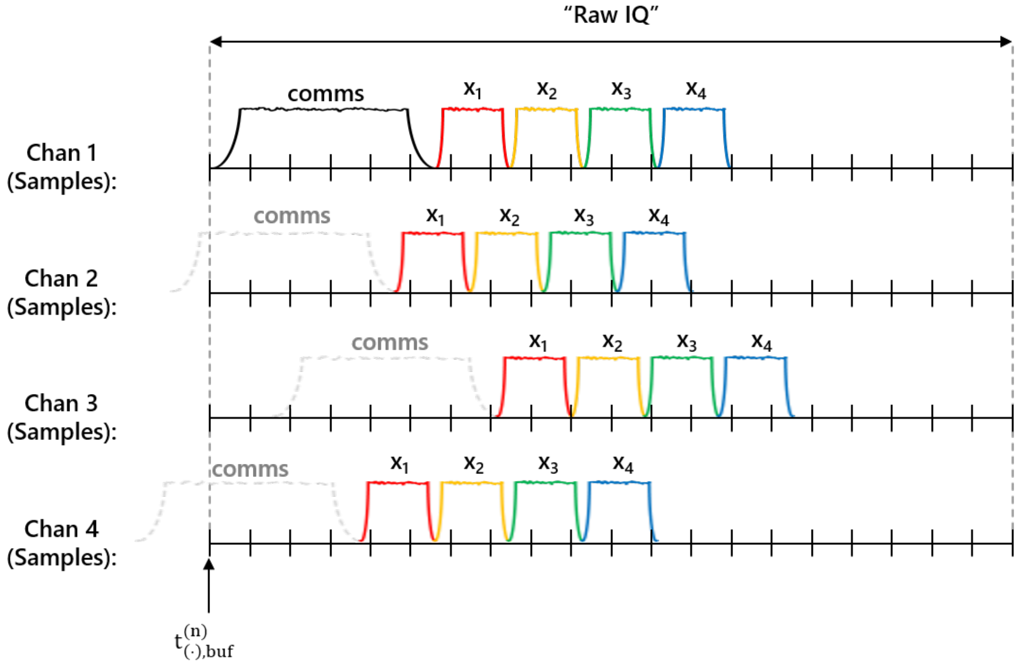

Figure 2.6: Depiction of the receiver frame detector.

2.3.3 Frequency Estimation

Due to imperfect clocks and propagation through the channel, a frequency offset will manifest in the received data. This offset negatively impacts both the accuracy of the ToA estimator and the decoding performance. This carrier frequency offset is estimated and corrected by the communications processing chain before decoding the message. This estimator measures the phase of each amble sequence and computes the difference to estimate the frequency offset. Two frequency corrections are applied to the incoming data. The first is a coarse correction used to decode the communications payload. The second is a fine correction used to maximize the performance of the massive correlator.

Chapter 3

MODEL DEFINITIONS

I define high-fidelity time and propagation models upon which the ToA estimators and time synchronization algorithm are built. The time model describes the relationship between two radio platforms operating with independent clock sources, including a discussion of how clock drift and time-of-flight affect the timing of a received signal. The propagation model describes the physical and temporal distortions of a waveform as it travels from one radio to another, including attenuation, time shifts, phase offsets, and frequency dilation caused by Doppler and clock drift.

3.1 Time Model

I model the interaction between two distributed radios operating with independent, unsycnchronized clock sources. The independent behavior of these clocks induce phase offsets and frequency shifts in the received data. To accurately estimate the ToA of the received waveforms, we must carefully account for the nature of these oscillators.

3.1.1 Temporal Variables

Denote a master radio A and slave radio B. Define an event as any interaction between these radios. Define an event timestamp as the time at which an event occurs, according to the radio that percieves the event. Denote an event timestamp as

$$t^{(\cdot)}_{(\cdot),(\cdot)}, \tag{3.1}$$

where the first subscript indicates which radio experienced the event (A/B), the second subscript indicates the type of event (Tx/Rx) and the superscript indexes the events as defined below.

The primary objective of the positioning subsystem is to measure the distance between the antennas, d. A transmission from A to B will take approximately τ seconds to propagate, where $\tau = d/c$ and c is the speed of light in the medium. If the clock sources for radios A and B were perfectly aligned, τ could be estimated directly by finding the difference in the transmit and receive timestamps. For misaligned clocks, define an offset T between the times displayed on clocks A and B at a given instant. By convention, define a positive T as clock B displaying an earlier time than clock A, such that

$$t_{B,(\cdot)}^{(\cdot)} = t_{A,(\cdot)}^{(\cdot)} - T. \tag{3.2}$$

To estimate τ, the radios alternate transmitting and receiving a joint positioning-communications waveform, as depicted in Figure 3.1. T and τ are then jointly estimated to simultanesouly synchronize the clocks and estimate the distance between the platforms.

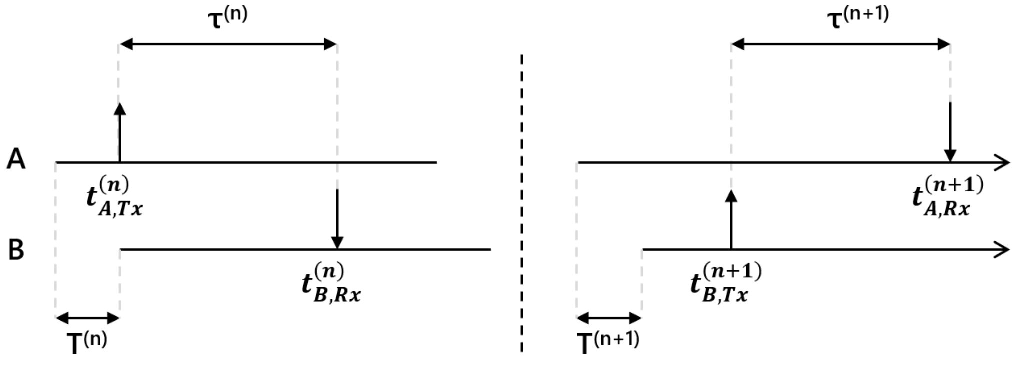

Figure 3.1: Depiction of two interactions between radios A and B. The first interaction (indexed by n) consists of a transmit event at A and a receive event at B. The second interactions consists of a transmit event at B and a receive event at A.

Define a state space containing the time-of-flight τ, time offset T, and their first order derivatives $\dot{\tau}$ and $\dot{T}$. Define a set of N time frames indexed by n. Assume that each time frame contains at most one interaction between radios A and B. Enumerate the state space as the instantaneous values of each variable at the start of each frame. For a given frame, denote the instantaneous values of the state space variables as $\tau^{(n)}$, $T^{(n)}$, $\dot{\tau}^{(n)}$, and $\dot{T}^{(n)}$. Model the time-of-flight in frame n as

$$\tau^{(n)} = \tau^{(n-1)} + \dot{\tau}^{(n-1)} l^{(n-1)}, \tag{3.3}$$

where $l^{(n-1)}$ is the duration of the previous frame. Model the time offset T as

$$T^{(n)} = T^{(n-1)} + \dot{T}^{(n-1)} l^{(n-1)}. \tag{3.4}$$

The quality of this model diminishes with increasing frame length l and nontrivial higher order derivatives.

3.1.2 Transmission and Reception

Event timestamps are the primary measurement by which the radios gain information about the state space. I model the relationship between these event timestamps and the state space variables below.

Every transmit and receive event has a corresponding timestamp. Transmit timestamps are chosen by the transmitter. Receive timestamps are estimated at the receiver. For a transmission from A to B, the receive timestamp is modeled as

$$t_{B,Rx}^{(n)} = t_{A,Tx}^{(n)} + \tau^{(n)} - T^{(n)}. \tag{3.5}$$

For a transmission from B to A, the receive timestamp is modeled as

$$t_{A,Rx}^{(n)} = t_{B,Tx}^{(n)} + \tau^{(n)} + T^{(n)}. \tag{3.6}$$

These equations are the basis for the ToA estimation techniques and the time syncronization algorithm.

3.1.3 Nominal Frequency Mismatch

Radios A and B are driven by independent, unsynchronized clocks. These clocks are expected to operate at some nominal frequencies $f_{\{clock,nominal,A\}}$ and $f_{\{clock,nominal,B\}}$. These clocks are imperfect, however, so the actual frequencies differ from the nominal frequencies by some errors ϵ_A and ϵ_B, such that

$$f_{\{clock,actual,A\}} \triangleq f_{\{clock,nominal,A\}} + \epsilon_A, \tag{3.7}$$

$$f_{\{clock,actual,B\}} \triangleq f_{\{clock,nominal,B\}} + \epsilon_B, \tag{3.8}$$

Limits on these error terms are usually given in the specifications sheet of the oscillator. Behavior within these limits will depend on the type and quality of the oscillator. These clocks do not necessarily operate at the same nominal frequency, so define a conversion term α such that

$$f_{\{clock,nominal,B\}} \triangleq \alpha f_{\{clock,nominal,A\}}. \tag{3.9}$$

The error terms ϵ_A and ϵ_B cannot be measured directly; this would require a perfect reference clock. The *difference* between the actual clock frequencies, however, can be estimated directly. It is useful to consider the clock drift $\dot{T}$ in terms of the actual and nominal clock frequencies, such that

$$\dot{T} \triangleq \frac{f_{\{cl,ac,A\}}}{f_{\{cl,n,A\}}} - \frac{f_{\{cl,ac,B\}}}{f_{\{cl,n,B\}}}. \tag{3.10}$$

This represents the difference between the two actual frequencies, converted to units of seconds per second. This formulation is useful because $\dot{T}$ can be estimated directly, as discussed later in this report, and it provides insight on how this variable affects the propagation characteristics. By substituting (3.7) and (3.8), this can be expressed in terms of ϵ_A and ϵ_B as

$$\begin{aligned}\dot{T} &\triangleq \frac{f_{\{cl,ac,A\}}}{f_{\{cl,n,A\}}} - \frac{f_{\{cl,ac,B\}}}{f_{\{cl,n,B\}}}, \\ &= \frac{f_{\{cl,n,A\}} + \epsilon_A}{f_{\{cl,n,A\}}} - \frac{f_{\{cl,n,B\}} + \epsilon_B}{f_{\{cl,n,B\}}}, \\ &= 1 + \frac{\epsilon_A}{f_{\{cl,n,A\}}} - 1 - \frac{\epsilon_B}{f_{\{cl,n,B\}}}, \\ &= \frac{\epsilon_A}{\frac{1}{\alpha} f_{\{cl,n,B\}}} - \frac{\epsilon_B}{f_{\{cl,n,B\}}}, \\ &= \frac{\alpha\epsilon_A - \epsilon_B}{f_{\{cl,n,B\}}}. \end{aligned} \tag{3.11}$$

The actual frequencies can then be expressed in terms of $\dot{T}$ such that

$$\begin{aligned} f_{\{cl,n,A\}} &\triangleq f_{\{cl,ac,A\}} - \epsilon_A; \\ f_{\{cl,n,B\}} &\triangleq \alpha f_{\{cl,n,A\}}, \\ &= \alpha\left(f_{\{cl,ac,A\}} - \epsilon_A\right); \\ f_{\{cl,ac,B\}} &\triangleq f_{\{cl,n,B\}} + \epsilon_B \\ &= \alpha\left(f_{\{cl,ac,A\}} - \epsilon_A\right) + \epsilon_B, \\ &= \alpha f_{\{cl,ac,A\}} + \left(\epsilon_B - \alpha\epsilon_A\right), \\ &= \alpha f_{\{cl,ac,A\}} - f_{\{cl,n,B\}}\dot{T}. \end{aligned} \tag{3.12}$$

This error is propagated when the clock frequencies are multiplexed to synthesize the carrier frequencies. We assume that both radios operate at the same carrier frequency, thus

$$f_{\{cr,n,A\}} = f_{\{cr,n,B\}} \tag{3.13}$$

Define the multiplexing factors

$$\gamma \triangleq \frac{f_{\{cr,n,A\}}}{f_{\{cl,n,A\}}}, \tag{3.14}$$

$$\begin{aligned}\beta &\triangleq \frac{f_{\{cr,n,B\}}}{f_{\{cl,n,B\}}} && (3.15)\\ &= \frac{f_{\{cr,n,A\}}}{\alpha f_{\{cl,n,A\}}} \\ &= \frac{\gamma}{\alpha}. && (3.16)\end{aligned}$$

Thus,

$$f_{\{carrier,actual,A\}} = \gamma f_{\{clock,actual,A\}}, \tag{3.17}$$

$$f_{\{carrier,actual,B\}} = \beta f_{\{clock,actual,B\}}. \tag{3.18}$$

The previous clock errors propagate through this multiplexing.

$$\begin{aligned}f_{cr,ac,B} &= \beta f_{\{cl,ac,B\}} \\ &= \beta\left(\alpha f_{\{cl,ac,A\}} - f_{\{cl,n,B\}}\dot{T}\right) \\ &= \gamma f_{\{cl,ac,A\}} - \beta f_{\{cl,n,B\}}\dot{T} && (3.19)\\ &= f_{\{cr,ac,A\}} - \beta f_{\{cl,n,B\}}\dot{T} && (3.20)\end{aligned}$$

Consider a relative velocity between the two platforms v. Define v^+ as a relative velocity such that the platforms are moving away from each other, and $v^- = -v^+$. Define the first derivative of τ as

$$\begin{aligned}\dot{\tau} &\triangleq \frac{\Delta\tau}{\Delta t} && (3.21)\\ &= \frac{\Delta d}{c\Delta t} \\ &= \frac{v^+}{c} && (3.22)\end{aligned}$$

If there is relative velocity between the platforms, a Doppler frequency shift will be induced such that

$$f_{\{cr,dop,Tx\}} = \left(1 + \frac{v^-}{c}\right) f_{\{cr,ac,Tx\}}, \tag{3.23}$$

$$= \left(1 - \dot{\tau}\right) f_{\{cr,ac,Tx\}}, \tag{3.24}$$

3.1.4 Cross-Platform Frequency Mismatch

When a signal is upconverted to passband and transmitted between radios with different clock sources, there will be some error in the downconversion at the receiver, because the received frequency, $f_{\{cr,dop,Tx\}}$, will not exactly match the receiver synthesized frequency, $f_{\{cr,ac,Rx\}}$. This difference may be estimated directly, discussed later in this report. This difference may also be expressed in terms of the state space variables $\dot{\tau}$ and $\dot{T}$.

Frequency Mismatch, A to B

Assume that node A is the transmitter and node B is the receiver.

$$\begin{aligned}
f_{\{cr,dop,A\}} - f_{\{cr,ac,B\}} &= (1-\dot{\tau})f_{\{cr,ac,A\}} - f_{\{cr,ac,B\}} \\
&= (1-\dot{\tau})\left(f_{\{cr,ac,B\}} + \beta f_{\{cl,n,B\}}\dot{T}\right) - f_{\{cr,ac,B\}} \\
&= (1-\dot{\tau})f_{\{cr,ac,B\}} + (1-\dot{\tau})\beta f_{\{cl,n,B\}}\dot{T} - f_{\{cr,ac,B\}} \\
&= \beta(1-\dot{\tau})\dot{T} f_{\{cl,n,B\}} - \dot{\tau} f_{\{cr,ac,B\}} \qquad (3.25) \\
&= \xi_B - \dot{\tau} f_{\{cr,ac,B\}} \qquad (3.26) \\
&= \zeta_B \qquad (3.27)
\end{aligned}$$

Frequency Mismatch, B to A

Assume that node B is the transmitter and node A is the receiver.

$$\begin{aligned}
f_{\{cr,dop,B\}} - f_{\{cr,ac,A\}} &= (1-\dot{\tau})f_{\{cr,ac,B\}} - f_{\{cr,ac,A\}} \\
&= (1-\dot{\tau})\left(f_{\{cr,ac,A\}} - \beta f_{\{cl,n,B\}}\dot{T}\right) - f_{\{cr,ac,A\}} \\
&= (1-\dot{\tau})f_{\{cr,ac,A\}} - (1-\dot{\tau})\beta f_{\{cl,n,B\}}\dot{T} - f_{\{cr,ac,A\}} \\
&= -\beta(1-\dot{\tau})\dot{T} f_{\{cl,n,B\}} - \dot{\tau} f_{\{cr,ac,A\}} \qquad (3.28) \\
&= \xi_A - \dot{\tau} f_{\{cr,ac,B\}} \qquad (3.29) \\
&= \zeta_A \qquad (3.30)
\end{aligned}$$

3.2 Propagation Model

I define and model the characteristics of a waveform transmitted through free space between two radios operating with unsynchronized clock sources. This waveform will undergo a time delay, phase shift, frequency shift, and channel attenuation. I model the transmission characteristics for a single-input single-output (SISO) waveform between unsynchronized radios.

3.2.1 Synthesis

The transmitter prepares a transmission by synthesizing a baseband waveform $x_0(t)$. This waveform contains both a communications payload and navigation reference sequences. The subscript 0 indicates that the waveform starts at time index 0, and more specifically:

$$|x_0(t)|^2 = 0 \ \forall \ t \notin \ [0, T_{x_0}], \tag{3.31}$$

where T_{x_0} is the duration of the waveform in seconds and t is a nominal time reference. This waveform is then indexed by the time reference of the transmitter, t_{Tx}, and is transmitted at time $t^{(\cdot)}_{Tx,Tx}$, such that the baseband transmission $x_{bb}(t)$ is

$$x_{bb}(t_{Tx}) = x_0 \left(t_{Tx} - t^{(\cdot)}_{Tx,Tx} \right). \tag{3.32}$$

3.2.2 Transmission

Prior to transmission, the baseband waveform is up-converted to the transmitter carrier frequency. This up-conversion is modeled as

$$\begin{aligned} x_{pb}(t_{Tx}) &= x_{bb}(t_{Tx}) e^{j2\pi f_{\{cr,ac,Tx\}} t_{Tx}} && (3.33) \\ &= x_0 \left(t_{Tx} - t^{(\cdot)}_{Tx,Tx} \right) e^{j2\pi f_{\{cr,ac,Tx\}} t_{Tx}}. && (3.34) \end{aligned}$$

The passband signal travels through the hardware and is transmitted from an antenna with some potentially unknown phase ϕ_{Tx}, such that the actual waveform that enters the environment is modeled as

$$\begin{aligned} x_{Tx}(t_{Tx}) &= x_{pb}(t_{Tx}) e^{j2\pi \phi_{Tx}} && (3.35) \\ &= x_0 \left(t_{Tx} - t^{(\cdot)}_{Tx,Tx} \right) e^{j2\pi \left(\phi_{Tx} + f_{\{cr,ac,Tx\}} t_{Tx} \right)}. && (3.36) \end{aligned}$$

3.2.3 Propagation

As the transmission propagates from the transmission platform to the reception platform, it will undergo a Doppler frequency shift, complex attenuation, and time delay. If there is relative velocity between the platforms, a Doppler frequency shift will be induced according to Equation (3.23). For a narrowband waveform, this effect is modeled by

$$x_{Tx}(t_{Tx}) = x_0 \left(t_{Tx} - t^{(\cdot)}_{Tx,Tx} \right) e^{j2\pi \left(\phi_{Tx} + f_{\{cr,dop,Tx\}} t_{Tx} \right)}. \tag{3.37}$$

The complex attenuation a induced by the channel is modeled as [65]

$$a = |a| e^{j2\pi \phi_a} \ , \ |a| = \sqrt{\frac{G_{Tx} G_{Rx} \lambda^2}{(4\pi d^2)}}; \tag{3.38}$$

where G_{Tx} and G_{Rx} are the transmitter and receiver gains, λ is the waveform wavelength, and d is the distance between the platforms. For simple line-of-sight channels, we assume that $\phi_a \approx 0$. The time of propagation τ induces a time shift such that the waveform impinges upon the receiver at time $t^{(\cdot)}_{Tx,Tx} - \tau$:

$$z_{pb}(t_{Tx}) = |a| e^{j2\pi\phi_a} x_{Tx}(t_{Tx} - \tau) \tag{3.39}$$

$$= |a| x_0 \left(t_{Tx} - t^{(\cdot)}_{Tx,Tx} - \tau\right) e^{j2\pi\left(\phi_{Tx}+\phi_a+f_{\{cr,dop,Tx\}}(t_{Tx}-\tau)\right)} \tag{3.40}$$

3.2.4 Reception

When the transmission is measured by the receiver, it is corrupted by noise, and we transition to the receiver time reference. The time conversion is defined by (3.2), thus the received signal referenced by the receiver clock is modeled as

$$z_{pb}(t_{Rx}) = |a| x_0 \left(t_{Rx} - t^{(\cdot)}_{Tx,Tx} - \tau \pm T\right) e^{j2\pi\left(\phi_{Tx}+\phi_a+f_{\{cr,dop,Tx\}}(t_{Rx}-\tau\pm T)\right)}, \tag{3.41}$$

where the sign is determined by which platform is receiving according to (3.2). This signal is measured by a receive antenna, with some potentially unknown phases ϕ_{Rx}, thus the received signal is modeled as

$$z_{pb}(t_{Rx}) = |a| x_0 (\sim) e^{j2\pi\left(\phi_{Tx}+\phi_a-\phi_{Rx}+f_{\{cr,dop,Tx\}}(t_{Rx}-\tau\pm T)\right)}, \tag{3.42}$$

At this point, it is useful to combine the phase terms into a single nuisance parameter $\tilde{\phi} = \phi_{Tx} + \phi_a - \phi_{Rx}$, such that (3.42) may be written as

$$z_{pb}(t_{Rx}) = |a| x_0 (\sim) e^{j2\pi\left(\tilde{\phi}+f_{\{cr,dop,Tx\}}(t_{Rx}-\tau\pm T)\right)}. \tag{3.43}$$

The random quantity $\tilde{\phi}$ may be estimated directly in a calibration setup discussed later. In the process of measuring this signal, the reception is contaminated by noise, here modeled as additive in amplitude, such that

$$z_{pb}(t_{Rx}) = |a| x_0 (\sim) e^{j2\pi\left(\tilde{\phi}+f_{\{cr,dop,Tx\}}(t_{Rx}-\tau\pm T)\right)} + n(t_{Rx}), \tag{3.44}$$

where $n(t_{Rx})$ is a random process. This is down-converted from pass-band by applying a band-pass filter and multiplying by $e^{\left(-j2\pi f_{\{cr,ac,Rx\}} t_{Rx}\right)}$, such that

$$z_{bb}(t_{Rx}) = |a| x_0 \left(\sim\right) e^{j2\pi\left(\tilde{\phi}+f_{\{cr,dop,Tx\}}(t_{Rx}-\tau\pm T)\right)} e^{\left(-j2\pi f_{\{cr,ac,Rx\}} t_{Rx}\right)} + n'(t_{Rx}), \qquad (3.45)$$

where n' is the filtered version of the noise process, assumed to be circularly symetric white Gaussian noise with zero mean and variance σ^2.

3.3 System Model

The propagation model defined in (3.45) may be expressed in terms of the state space variables defined in the previous section. I present an alternate expression that clearly identifies nuisance parameters and expresses the received signal in terms of variables that can either be measured or calibrated.

3.3.1 System Propagation, A to B

I simplify the propagation model defined in (3.45) assuming that node A is the transmitter and node B is the receiver. For notational simplicity, it is convenient to make the following substitutions (defined in Section 3.1.4):

$$\bar{\tau}_B = \tau - T, \tag{3.46}$$

$$\xi_B = \beta(1-\dot{\tau})\dot{T} f_{\{cl,n,B\}}, \tag{3.47}$$

$$\zeta_B = \xi_B - f_{\{cr,ac,B\}}\dot{\tau}. \tag{3.48}$$

Rewrite (3.45) in the form

$$\boxed{z_{bb}(t_B) = |a| x_0 \left(t_B - t^{(\cdot)}_{A,Tx} - \tau + T\right) e^{jp} + n'(t_B)}\,, \tag{3.49}$$

where p represents all of the phase terms, and can be simplified [1] , [2] as follows:

$$\begin{aligned}
p &= 2\pi\left(\tilde{\phi} + f_{\{cr,dop,A\}}(t_B - \tau + T)\right) + \left(-2\pi f_{\{cr,ac,B\}} t_B\right), \; ^{1}\\
&= 2\pi\left(\tilde{\phi} + f_{\{cr,dop,A\}}(t_B - \bar{\tau}_B) - f_{\{cr,ac,B\}} t_B\right),\\
&= 2\pi\left(\tilde{\phi} + \left(f_{\{cr,dop,A\}} - f_{\{cr,ac,B\}}\right) t_B - f_{\{cr,dop,A\}}\bar{\tau}_B\right),\\
&= 2\pi\left(\tilde{\phi} + \zeta_B t_B - f_{\{cr,dop,A\}}\bar{\tau}_B\right), \; ^{2}\\
&= 2\pi\left(\tilde{\phi} + \zeta_B t_B - \left(f_{\{cr,ac,B\}} + \zeta_B\right)\bar{\tau}_B\right),
\end{aligned}$$

$$\boxed{p = 2\pi\left(\tilde{\phi} + \zeta_B t_B - \left(f_{\{cr,n,B\}} + \epsilon_B + \zeta_B\right)\bar{\tau}_B\right)} \tag{3.50}$$

[1] Simplification of (3.45)

[2] Application of results of Section 3.1.4

3.3.2 System Propagation, B to A

I simplify the propagation model defined in (3.45) assuming that node B is the transmitter and node A is the receiver. For notational simplicity, it is convenient to make the following substitutions (defined in Section 3.1.4):

$$\bar{\tau}_A = \tau + T, \tag{3.51}$$

$$\xi_A = -\beta(1-\dot{\tau})\dot{T} f_{\{cl,n,B\}}, \tag{3.52}$$

$$\zeta_A = \xi_A - f_{\{cr,ac,A\}}\dot{\tau}. \tag{3.53}$$

We rewrite (3.45) in the form

$$\boxed{z_{bb}(t_A) = |a| x_0 \left(t_A - t_{B,Tx}^{(\cdot)} - \tau - T\right) e^{jp} + n'(t_A)}\ , \tag{3.54}$$

where p represents all of the phase terms, and can be simplified [3] , [4] as follows:

$$\begin{aligned} p &= 2\pi\left(\tilde{\phi} + f_{\{cr,dop,B\}}(t_A - \tau - T)\right) + \left(-2\pi f_{\{cr,ac,A\}} t_A\right), \ ^3 \\ &= 2\pi\left(\tilde{\phi} + f_{\{cr,dop,B\}}(t_A - \bar{\tau}_A) - f_{\{cr,ac,A\}} t_A\right), \\ &= 2\pi\left(\tilde{\phi} + \left(f_{\{cr,dop,B\}} - f_{\{cr,ac,A\}}\right) t_A - f_{\{cr,dop,B\}}\bar{\tau}_A\right), \\ &= 2\pi\left(\tilde{\phi} + \zeta_A t_A - f_{\{cr,dop,B\}}\bar{\tau}_A\right), \ ^4 \\ &= 2\pi\left(\tilde{\phi} + \zeta_A t_A - \left(f_{\{cr,ac,A\}} + \zeta_A\right)\bar{\tau}_A\right), \\ &= 2\pi\left(\tilde{\phi} + \zeta_A t_A - \left(f_{\{cr,n,A\}} + \epsilon_A + \zeta_A\right)\bar{\tau}_A\right). \end{aligned}$$

$$\boxed{p = 2\pi\left(\tilde{\phi} + \zeta_A t_A - \left(f_{\{cr,n,A\}} + \epsilon_A + \zeta_A\right)\bar{\tau}_A\right)} \tag{3.55}$$

[3] Simplification of (3.45)

[4] Application of results of Section 3.1.4

3.3.3 Carrier Phase Reset

To use the phase of a received signal to improve ToA estimates, we must be able to accurately predict the phase term in (3.50) and (3.55) at the chosen test points of $\bar{\tau}$. This becomes difficult to maintain, because the clock sources continuously evolve, so the frequency offset term ζt is non-linear. The above models assume that it is linear, so the true value drifts away from this linear prediction as the clocks evolve. In an attempt to mitigate this discrepancy, it is possible to reset the phase of the frequency synthesizer before and after transmissions. By resetting the synthesizer to a known phase just before transmission and reception, we can limit the window of opportunity for the true offset to drift away from the linear prediction, making the phase prediction more reliable. Unfortunately, this process also introduces phase noise in the transmitted signal, which may also diminish the performance of the ToA estimator. A study of how much phase noise this introduces and how much it impacts the system is a topic we will explore in future work.

If the transmitter resets its frequency synthesizer right at the transmit time $t^{(\cdot)}_{Tx,Tx}$, then (3.36) becomes

$$x_{Tx}(t_{Tx}) = x_0\left(t_{Tx} - t^{(\cdot)}_{Tx,Tx}\right) e^{j2\pi\left(\phi_{Tx} + f_{\{cr,ac,Tx\}}(t_{Tx} - t^{(\cdot)}_{Tx,Tx})\right)}. \tag{3.56}$$

The phase term p in (3.50) then becomes

$$\begin{aligned} p &= 2\pi\left(\tilde{\phi} + f_{\{cr,dop,A\}}(t_B - t^{(\cdot)}_{A,Tx} - \tau + T) - f_{\{cr,ac,B\}}t_B\right) \\ &= 2\pi\left(\tilde{\phi} + f_{\{cr,dop,A\}}(t_B - t^{(\cdot)}_{A,Tx} + T) - f_{\{cr,ac,B\}}t_B - f_{\{cr,dop,A\}}\tau\right) \\ &= 2\pi\left(\tilde{\phi} + f_{\{cr,dop,A\}}(t_A - t^{(\cdot)}_{A,Tx}) - f_{\{cr,ac,B\}}t_B - f_{\{cr,dop,A\}}\tau\right) \end{aligned} \tag{3.57}$$

We are primarily concerned with the phase corresponding to the time at which the waveform first impinges upon the receive antenna. This time, as perceived by the transmitter (A) is denoted $\tilde{t}^{(\cdot)}_{A,Rx}$, where the tilde denotes that the timestamp belongs to the radio that did not experience the corresponding event. Making this substitution.

$$\begin{aligned} p_{Rx} &= 2\pi \left(\tilde{\phi} + f_{\{cr,dop,A\}}(\tilde{t}^{(\cdot)}_{A,Rx} - t^{(\cdot)}_{A,Tx}) - f_{\{cr,ac,B\}}t_B - f_{\{cr,dop,A\}}\tau \right) \\ &= 2\pi \left(\tilde{\phi} + f_{\{cr,dop,A\}}(\tau) - f_{\{cr,ac,B\}}t_B - f_{\{cr,dop,A\}}\tau \right) \\ &= 2\pi \left(\tilde{\phi} - f_{\{cr,ac,B\}}t_B, \right) \end{aligned} \tag{3.58}$$

where p_{Rx} is the received phase at time $\tilde{t}^{(\cdot)}_{A,Rx}$. If the receiver also resets the phase of the carrier synthesizer at some time $t_{B,rst}$ right before reception,

$$p_{Rx} = 2\pi \left(\tilde{\phi} - f_{\{cr,ac,B\}}(t_B - t_{B,rst}) \right)$$

Again, we are only concerned with the phase at the time-of-arrival, so $t_B = t^{(\cdot)}_{B,Rx}$, thus

$$\begin{aligned} p_{Rx} &= 2\pi \left(\tilde{\phi} - f_{\{cr,ac,B\}}(t^{(\cdot)}_{B,Rx} - t_{B,rst}) \right) \\ &= \boxed{2\pi \left(\tilde{\phi} - f_{\{cr,ac,B\}}\delta \right)}\ , \end{aligned} \tag{3.59}$$

where $\delta = t^{(\cdot)}_{B,Rx} - t_{B,rst}$. If the ToA can be predicted well enough to make δ small, the phase for a given test point $(t^{(\cdot)}_{B,Rx})$ can be predicted accurately and used to significantly improve the performance of the ToA estimator. This is further predicated on the assumption that $\tilde{\phi}$ can be esimtated sufficiently well during calibration.

Chapter 4

TIME-OF-ARRIVAL ESTIMATION

I investigate several time-of-arrival estimation techniques according to the models defined in (3.49) and (3.54). The ToA may be coarsely estimated by optimizing an incoherent cost function that compares the received signal with a known reference waveform at different delay hypotheses. This estimate may be refined by increasing the sampling rate at which this optimization is performed, and further improved by interpolating the correlation results. If the phase of the received waveform can be predicted with sufficient accuracy, then the phase of the correlation may be used to refine the estimate even further. We discuss the technical challenges associated with including this phase information, and compare the theoretical and simulated performance of the proposed estimators.

4.1 Estimation Preliminaries

Time-of-arrival is the time at which a signal impinges upon a receiving antenna. In the context of the joint positioning-communications system, the ToA is equivalent to the received timestamp $t_{(\cdot),Rx}^{(\cdot)}$ as measured by the receiver. ToA estimation is well studied with application to many systems. This discussion, however, is a departure from traditional ToA estimation techniques, thus we carefully define our assumptions and goals to distinguish our results.

The traditional maximum-likelihood ToA estimator is a matched filter that compares the received signal with a known reference signal at different delay hypotheses. The received waveform is digitally sampled at the receiver, which imposes a fundamental limit on the resolution of this matched filter. Basic estimation techniques are limited to this resolution. More advanced techniques may surpass this resolution by oversampling the received and reference waveforms and estimating ToA in this oversampled space. These estimates may be further refined by leveraging the phase information of the received signal and knowledge shared by the transmitter. Define the following sampling frequencies:

Table 4.1: Estimation Variable Definitions

Label	Description	Equation
$f_{s,c}$	Critical Sampling Frequency	
$f_{s,f}$	Filtered Sampling Frequency	
$f_{s,sim}$	Simulation Sampling Frequency	
$f_{s,est}$	Estimator Sampling Frequency	
ρ_{sps}	Samples per Symbol	$\frac{f_{s,f}}{f_{s,c}}$
ρ_{sim}	Simulation Samples per Symbol	$\frac{f_{s,sim}}{f_{s,c}}$
ρ_{est}	Estimator Samples per Symbol	$\frac{f_{s,est}}{f_{s,c}}$

4.2 Coarse ToA Estimation

The coarse ToA estimator maximizes an objective function that is sampled at either the Nyquist sampling rate ($f_{s,c}$), or some small multiple thereof ($f_{s,f}$). Consider the incoherent objective function [1, 2]

$$g(\tau') = \left| \int dt \; z_{bb}(t) x_0^*(t - \tau') \right|^2 \tag{4.1}$$

This is is a matched filter that compares the received baseband signal $z_{bb}(t)$ with the known transmit signal $x_0(t)$ at different delay hypotheses τ'. By inspection of (3.45), this objective function is maximized for $\tau' = t_{Tx,Tx}^{(\cdot)} + \tau \mp T$, thus (3.5) and (3.6) indicate that the ML ToA estimate is simply

$$\hat{\tau}' = \arg\max_{\tau'} g(\tau'). \tag{4.2}$$

The receiver cannot record $z_{bb}(t)$ directly, and is forced to instead sample it such that

$$\mathbf{z}_{bb}[m] = z_{bb}\left(m f_{s,f}^{-1}\right) \;, \; m \in [0, 1, ..., M-1], \tag{4.3}$$

where m indexes the samples in $\mathbf{z}_{bb}$, M is the total number of collected samples, and $f_{s,f}^{-1}$ is the sampling period. The receiver must then approximate the objective function (4.1) as

$$\mathbf{g}(k) = \left| \sum_{m=0}^{M-1} \mathbf{z}_{bb}[m] \mathbf{x}_0^*[m-k] \right|^2 \;, \; k \in [0, 1, , ..., K-1]. \tag{4.4}$$

Assuming that $\mathbf{z}_{bb}$ is zero after $M-1$ samples, and that the receiver only saves the N preceding, nonzero samples, then this objective function only needs to be evaluated over these N samples:

$$\mathbf{g}(k) = \left| \sum_{m=M-N}^{M-1} \mathbf{z}_{bb}[m] \mathbf{x}_0^*[m-k] \right|^2 \;, \; k \in [0, 1, , ..., K-1]. \tag{4.5}$$

The scope of this maximization may be further limited by only evaluating values of k around the expected time-of-arrival, which may be roughly estimated if the transmit time is known. Assuming a nominal, sampled ToA $\bar{k} \in \mathbb{Z}$, and some small, integer number of samples $\delta \ll K$, the objective function is limited to

$$\mathbf{g}(k) = \left| \sum_{m=M-N}^{M-1} \mathbf{z}_{bb}[m]\mathbf{x}_0^*[m-k] \right|^2 \ , \ k \in [\bar{k}-\delta, \bar{k}-\delta+1, ..., \bar{k}+\delta]. \tag{4.6}$$

The coarse ToA estimator is thus

$$\hat{\tau}_c' = \hat{k} f_{s,f}^{-1} \ , \hat{k} = \arg\max_k \mathbf{g}(k). \tag{4.7}$$

This estimator is limited to the test points defined by the sampling frequency $f_{s,f}$. In general, the true value will not lie on this sampling lattice, so the accuracy is limited to the resolution between test points.

4.3 Fine ToA Estimation

The resolution of the coarse ToA estimator defined in (4.7) may be improved by performing the maximization at a higher sampling frequency, at the cost of increased computational complexity. By upsampling $\mathbf{z}_{bb}$ and $\mathbf{x}_0$ to a higher frequency $f_{s,est}$, the distance between adjacent test points is reduced, and the resolution of the maximization is increased. This approach has the following limitations:

- **Computational Complexity**: Increasing the sampling factor by a factor of ρ increases both the number of test points and the number of samples in each signal by ρ, resulting in a ρ^2 multiplicative increase in the number of complex multiplications needed to evaluate $\hat{\tau}_c'$. This expansion may be mitigated by reducing the range of test points or iteratively refining the search space, but will still suffer from a massive increase in computation time.

- **Imperfect Upsampling**: The upsampling process is imperfect, so the upsampled versions of $\mathbf{z}_{bb}$ and $\mathbf{x}_0$ are only approximations. This can introduce bias into the ToA estimator, and fundamentally limit the accuracy despite further increases in the sampling rate. Furthermore, upsampling is a computationally expensive operation.

We mitigate these limitations by pre-designing a bank of shifted versions of the reference waveform $\mathbf{x}_0$ for a specific sampling frequency $f_{s,est}$. Instead of upsampling the reference waveform and computing the shifts in real time after each reception, the receiver instead multiplies the received signal by the correlator bank to compute the objective function.

The objective of this correlator bank is to allow the receiver to test delay hypotheses that lie on a fine sampling lattice ($f_{s,est}$), but only perform multiplication at the coarse sampling frequency ($f_{s,f}$). Consider a delay hypothesis $\bar{k}$ and a range of hypotheses around it, such that $k \in [\bar{k}-\delta, \bar{k}-\delta+1, ..., \bar{k}+\delta]$, all of which lie on the fine sampling lattice defined by $f_{s,est}$. Upsample $\mathbf{x}_0$ to $f_{s,est}$. Define the correlator bank $\mathbf{X}_0$ as

$$\mathbf{X}_0 = \begin{bmatrix} \rule[0.5ex]{2em}{0.4pt} & \mathbf{x}_0[m+\delta] & \rule[0.5ex]{2em}{0.4pt} \\ \rule[0.5ex]{2em}{0.4pt} & \mathbf{x}_0[m+\delta-1] & \rule[0.5ex]{2em}{0.4pt} \\ & \vdots & \\ \rule[0.5ex]{2em}{0.4pt} & \mathbf{x}_0[m+1] & \rule[0.5ex]{2em}{0.4pt} \\ \rule[0.5ex]{2em}{0.4pt} & \mathbf{x}_0[m] & \rule[0.5ex]{2em}{0.4pt} \\ \rule[0.5ex]{2em}{0.4pt} & \mathbf{x}_0[m-1] & \rule[0.5ex]{2em}{0.4pt} \\ & \vdots & \\ \rule[0.5ex]{2em}{0.4pt} & \mathbf{x}_0[m-\delta-1] & \rule[0.5ex]{2em}{0.4pt} \end{bmatrix}$$

$$= \begin{bmatrix} \mathbf{x}_0[\delta] & \mathbf{x}_0[\delta+1] & \cdots & \mathbf{x}_0[N] & 0 & \cdots & 0 \\ \mathbf{x}_0[\delta-1] & \mathbf{x}_0[\delta] & \ddots & \mathbf{x}_0[N-1] & \mathbf{x}_0[N] & \cdots & 0 \\ \mathbf{x}_0[\delta-2] & \mathbf{x}_0[\delta-1] & \ddots & \mathbf{x}_0[N-2] & \mathbf{x}_0[N-1] & \cdots & 0 \\ \ddots & \ddots & \ddots & \ddots & \ddots & \ddots & \ddots \\ \mathbf{x}_0[0] & \mathbf{x}_0[1] & \cdots & \mathbf{x}_0[N-\delta] & \mathbf{x}_0[N-\delta+1] & \cdots & \mathbf{x}_0[N-1] \\ 0 & \mathbf{x}_0[0] & \ddots & \mathbf{x}_0[N-\delta-1] & \mathbf{x}_0[N-\delta] & \ddots & \mathbf{x}_0[N-2] \\ \vdots & \ddots & \ddots & \ddots & \ddots & \ddots & \ddots \\ 0 & 0 & \ddots & \mathbf{x}_0[N-2\delta] & \mathbf{x}_0[N-2\delta+1] & \ddots & \mathbf{x}_0[N-\delta-1] \end{bmatrix}. \tag{4.8}$$

Each row of this matrix is a shifted version of the reference signal $\mathbf{x}_0$, such that each adjacent row is shifted by 1 sample at the oversampled frequency $f_{s,est}$. We then independently downsample each row to the processing sampling frequency $f_{s,f}$. The result is a new correlator bank $\mathbf{B}_0$, where the adjacent rows are still separated by 1 sample at $f_{s,est}$, but the signal within a row is sampled at the processing sampling frequency $f_{s,f}$. This allows us to test shifts at the higher sampling frequency but only perform multiplications at the lower sampling frequency. This improves the resolution of the correlator while mitigating the computational complexity. The new correlator bank is depicted in Figure 4.1.

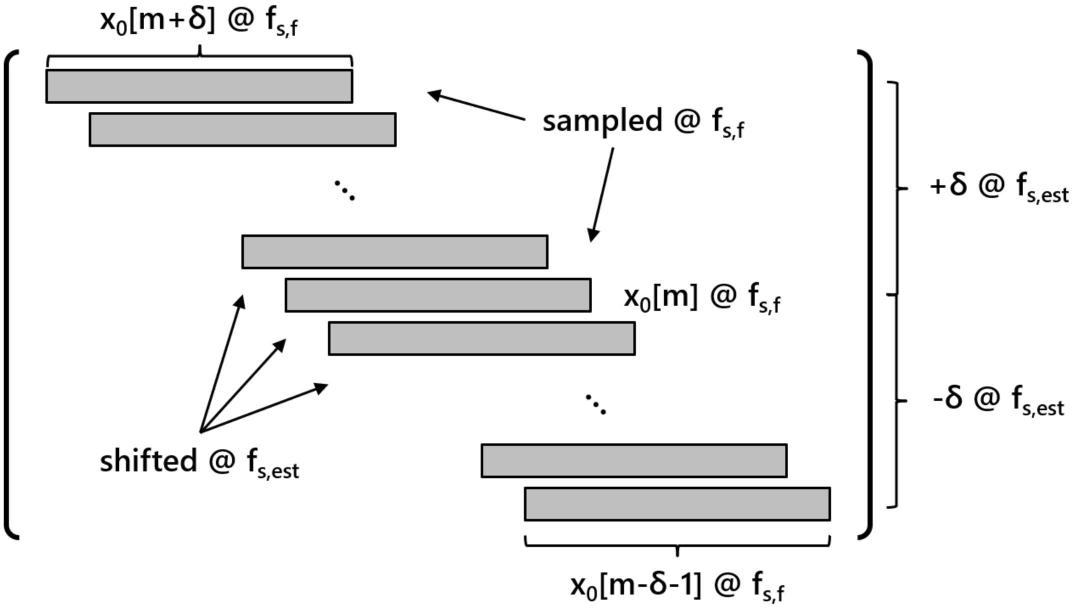

Figure 4.1: Depiction of the correlator bank $\mathbf{B}_0$. Adjacent rows are separated by a single sample shift at the oversampled sampling frequency $f_{s,est}$. Each signal within a row is downsampled to the processing sampling frequency $f_{s,f}$. This enables testing shifts at the oversampled resolution but only having to do multiplication at the lower processing sampling frequency, increasing resolution with a minimal increase in computational complexity.

The objective function (4.6) can be rewritten as a matrix multiplication with this correlator bank. The correlation must first be aligned such that the correlator bank rows correspond to the correct indeces in the objective function. This may be accomplished by performing a change of variables with $m' = m - \bar{k}$, such that

$$\mathbf{g}(k) = \left| \sum_{m'=M-N-\bar{k}}^{M-1-\bar{k}} \mathbf{z}_{bb}[m' + \bar{k}]\mathbf{x}_0^*[m' + \bar{k} - k] \right|^2, \; k \in [\bar{k} - \delta, \bar{k} - \delta + 1, ..., \bar{k} + \delta]. \quad (4.9)$$

By noting that k is defined as the set of shifts around $\bar{k}$, we can make another change of variables $k' = k - \bar{k} \in [-\delta, -\delta + 1, ..., \delta]$, such that

$$\mathbf{g}(k') = \left| \sum_{m'=M-N-\bar{k}}^{M-1-\bar{k}} \mathbf{z}_{bb}[m' + \bar{k}]\mathbf{x}_0^*[m' - k'] \right|^2 \ , \ k' \in [-\delta, -\delta + 1, ..., \delta]. \tag{4.10}$$

We may choose the central test point $\bar{k}$ at our convenience. In this case, the objective function (4.10) is evaluated at the processing sampling frequency $f_{s,f}$, and the frame detector is able to accurately locate the time of arrival to within 1 sample in this domain. It is therefore convenient to choose $\bar{k} = M - N$, i.e. the last N samples in the recorded signal where we assume the transmission resides. In this case, the objective function simplifies to

$$\mathbf{g}(k') = \left| \sum_{m'=0}^{N-1} \mathbf{z}_{bb}[m' + \bar{k}]\mathbf{x}_0^*[m' - k'] \right|^2 \ , \ k' \in [-\delta, -\delta + 1, ..., \delta]. \tag{4.11}$$

The limits of summation now align with the expression of the correlator bank in (4.8), so this operation may now be written in terms of a matrix multiplication. By defining $\mathbf{z}_f[m'] = \mathbf{z}_{bb}[m' + \bar{k}]$, i.e. the last N samples in the received sequence $\mathbf{z}_{bb}$ starting at sample $\bar{k}$, the objective function can now be written as

$$\mathbf{g}(k') = \mathbf{z}_f \mathbf{B}_0^{\dagger}, \tag{4.12}$$

where $\mathbf{B}_0$ is the downsampled version of $\mathbf{X}_0$. Both $\mathbf{z}_f$ and $\mathbf{B}_0$ are sampled at the coarse sampling frequency $f_{s,f}$, but the shifts k' are at the fine sampling frequency $f_{s,est}$. The ToA estimate may then be extracted from $\mathbf{g}(k')$ as the sum of $\bar{k}$ and k' both normalized to seconds, such that

$$\hat{\tau}_f' = \bar{k} f_{s,f}^{-1} + \hat{k}' f_{s,est}^{-1} \ , \ \hat{k}' = \arg\max_{k'} \mathbf{g}[k']. \tag{4.13}$$

This form allows for negative indeces k'. If it is necessary for $\mathbf{g}$ to be indexed by positive integers, then we may apply another change of variables $k'' = k' + \delta \in [0, 1, ..., 2\delta]$, and the estimate is appropriately shifted

$$\hat{\tau}_f' = \bar{k} f_{s,f}^{-1} + \left(\hat{k}'' - \delta \right) f_{s,est}^{-1} \ , \ \hat{k}'' = \arg\max_{k''} \mathbf{g}[k'']. \tag{4.14}$$

4.4 Correlator Interpolation

Time-of-arrival was previously estimated by finding the peak of the massive correlator. We now use several samples around the peak to estimate a 2nd order polynomial fit, and use this model to estimate the maximum likelihood ToA. The previous peak detection method limits the estimator to test points on the sampling lattice, but this interpolation method allows us to estimate the ToA without this quantization.

The interpolator is built by finding the peak value of the massive correlator, then taking a fixed number of preceeding and proceeding samples, and applying a least-squares 2nd order polynomial fit. Label the correlator indeces x_n, the corresponding correlation value y_n, and the index of the peak x_p. Consider M preceeding and proceeding samples around x_p, and build the arrays:

$$\mathbf{X} = \begin{bmatrix} x_{p-M}^2 & x_{p-M} & 1 \\ x_{p-M+1}^2 & x_{p-M+1} & 1 \\ \vdots & \vdots & \vdots \\ x_p^2 & x_p & 1 \\ \vdots & \vdots & \vdots \\ x_{p+M-1}^2 & x_{p+M-1} & 1 \\ x_{p+M}^2 & x_{p+M} & 1 \end{bmatrix}, \quad \mathbf{y} = \begin{bmatrix} y_{p-M} \\ y_{p-M+1} \\ \vdots \\ y_p^2 \\ \vdots \\ y_{p+M-1}^2 \\ y_{p+M}^2 \end{bmatrix}, \quad \mathbf{a} = \begin{bmatrix} a \\ b \\ c \end{bmatrix},$$

where a, b, c are the coefficients of the polynomial fit of the form $y = ax^2 + bx + c$. Using a least-squares solver to solve the system $\mathbf{y} = \mathbf{aX}$ produces estimates of these coefficients, and the vertex may be estimated directly as $-b/(2a)$. This vertex x_v replaces the peak value x_p as the new estimate of the ToA.

4.5 Phase Compensation

The fine ToA estimation technique significantly improves the accuracy of the estimates, but is still fundamentally limited by the choice of estimator sampling frequency. Under certain conditions, the phase of the objective function (4.12) may be leveraged to further improve the accuracy of the estimate. This phase is determined by the propagation characteristics, modeled in (3.49) and (3.54). Given a chosen test point $\hat{\tau}'$, we can estimate what the phase of the objective function should be at that point. If these two phases are different, we know that the test point is slightly off of the true value, and the difference in phases can be used to estimate this slight error.

Consider the phase term in (3.50). $\tilde{\phi}$ may be estimated using a calibration process, and ζ may be estimated using a standard frequency estimator and the pilot sequences in the communications payload. The nominal carrier frequency is known, and the error term ϵ is unknown and immeasurable. Define an estimate of the phase $\hat{p}'$ at test point $\hat{\tau}'$ as

$$\begin{aligned} \hat{p}' &= 2\pi \left(\hat{\tilde{\phi}} - \left(f_{\{cr,n,B\}} + \hat{\zeta} \right) \hat{\bar{\tau}} \right), \\ &= 2\pi \left(\hat{\tilde{\phi}} - \left(f_{\{cr,n,B\}} + \hat{\zeta} \right) \left(\hat{\tau}' - t^{(\cdot)}_{Tx,Tx} \right) \right). \end{aligned} \tag{4.15}$$

The phase of the objective function is approximately equal to (3.50), if the ζt term is ignored, thus

$$\arg(\mathbf{g}) = 2\pi \left(\tilde{\phi} - \left(f_{\{cr,n,B\}} + \epsilon + \zeta \right) \bar{\tau} \right). \tag{4.16}$$

By comparing the expected phase, $\hat{p}'$, and the measured phase, $\arg(\mathbf{g})$, we can extract an estimate of $\hat{\bar{\tau}} - \bar{\tau}$, which is the difference between the test point and true value. This is expressed explicitly as

$$\begin{aligned} \arg(\mathbf{g}) - \hat{p}' &= 2\pi \left(\tilde{\phi} - \hat{\tilde{\phi}} - \left(f_{\{cr,n,B\}} + \epsilon + \hat{\zeta} \right) \bar{\tau} + \left(f_{\{cr,n,B\}} + \hat{\zeta} \right) \hat{\bar{\tau}} \right), \\ &\approx 2\pi \left(\left(f_{\{cr,n,B\}} + \hat{\zeta} \right) \left(\hat{\bar{\tau}} - \bar{\tau} \right) \right), \end{aligned} \tag{4.17}$$

The time of arrival estimate may then be adjusted by this difference, such that the final phase compensated estimator is

$$\hat{\tau}'_p = \hat{\tau}'_f - \frac{\arg(\mathbf{g}) - \hat{p}'}{2\pi\left(f_{\{cr,n,B\}} + \hat{\zeta}\right)} \tag{4.18}$$

This process only improves performance under the following assumptions:

1. Sub-Cycle Accuracy: The carrier frequency for this system is 100 times greater than the bandwidth, which means that the carrier waveform will rotate 100 times between each sample. The phase at the output of the matched filter is therefore ambiguous across all of the cycles between two test samples. To disambiguate this, the time-of-arrival estimate must already be accurate to within a fraction of a sample, otherwise including the information makes the estimate strictly worse.

2. High Integrated SNR: To achieve the required sub-cycle accuracy with the fine estimator, the system must operate at high integrated SNR, as demonstrated in the following section.

3. Frequency Alignment: In order to know what the received phase should be, the transmitter and receiver clocks must either be aligned, or the misalignment must be known. There is a phase dilation associated with misaligned clocks that must be estimated before the phase information can be used. Without a mechanism to synchronize these clocks, this estimator is not viable.

4. Phase Calibration: The simplification above requires that the phase term $\tilde{\phi}$ has been estimated well. This must be done during a calibration process before this estimator can be implemented.

4.6 Performance Bounds

I characterize the performance of the following estimators:

1. Basic Cross Correlator - Performs a cross correlation of the received data and the reference waveform at the sampling frequency $f_{s,f} = 40$ MHz.

2. Massive Correlator - Performs a cross correlation using the massive correlator technique described above. The entries in the bank are sampled at $f_{s,f} = 40$ MHz and shifted at $f_{s,est} = 2$ GHz.

3. Interpolated Massive Correlator - Takes the correlation of the massive correlator and interpolates around the peak using $N = 15$ samples centered at the peak and the 2nd order interpolation method defined above.

4. Phase Refinement w/ Guess Reset - Takes the uninterpolated massive correlator ouptut and uses the phase to adjust the estimate of the maximum. This assumes that the phase has been reset according to (3.59). The simulated results assume that delta is a normal random variable with mean 1 ms and standard deviation 0.1 ms.

5. Phase Refinement w/ Truth - Phase refinement estimator without carrier phase reset, but instead assuming that the true value of the phase at each test point is simply known. This is used to demonstrate an absolute best-case scenario for the phase refinement class of estimators, but does not actually represent the achievable performance of any practical estimator.

4.6.1 Cramer-Rao Lower Bounds

The performance of these estimators may be characterized by the Cramér-Rao lower bound (CRLB), which is is a lower bound on the variance of an unbiased estimator. The above estimators may be catergorized into two classes: magnitude estimators and phase refinement estimators. The CRLBs for these estimators are well known, and specifically studied in [1, 2]. They are reproduced below with appropriate definitions.

Consider a perfectly band-limited complex signal s such that the Fourier transform $|S(f)|^2 = 0 \ \forall \ f \notin [-B/2, B, 2]$. In Circularly-Symmetric Additive White Guassian noise (CCAWGN) with variance σ^2, the CRLB on the variance of a ToA magnitude estimator is

$$\boxed{\mathrm{var}(\hat{\tau}) \geq \frac{1}{8\pi\rho B_{rms}^2}}\ , \tag{4.19}$$

where ρ is the integrated signal-to-noise ratio (SNR) and B_{rms}^2 is the root mean square (RMS) bandwidth squared. I explicitely define the integrated SNR to avoid any confusion:

$$\rho = \mathrm{ISNR} = \frac{\epsilon B}{\sigma^2} \ \ ; \ \ \epsilon = \int_{-\infty}^{\infty} dt \ |s(t)|^2. \tag{4.20}$$

Furthermore,

$$B_{rms}^2 = \frac{\int_{-\infty}^{\infty} df \ f^2 |S(f)|^2}{\int_{-\infty}^{\infty} df \ |S(f)|^2}. \tag{4.21}$$

The CRLB on a correpsonding phase refinement estimator is

$$\boxed{\operatorname{var}(\hat{\tau}) \geq \frac{1}{8\pi\rho f_{rms}^2}}, \tag{4.22}$$

$$f_{rms}^2 = \frac{\int_{-\infty}^{\infty} df \ (f + f_c)^2 |S(f)|^2}{\int_{-\infty}^{\infty} df \ |S(f)|^2}. \tag{4.23}$$

4.6.2 Simulated Results

The five estimators mentioned above are simulated in a Monte Carlo simulation environment. The results are plotted in Figure 4.2 alongside the two CRLBs (4.19) and (4.22). The critically sampled correlator (red/dot) plateaus once it reaches the intrinsic resolution of the sampling lattice defined by $f_{s,f}$. The massive correlator (yellow/x) similarly plateus at the higher resolution defined by $f_{s,est}$. The interpolation estimator (green/square) improves the massive correlator result by about a factor of 10 at high SNR. The phase refinement estimator with true knowledge of the phase (purple/triangle) does not reach the corresponding CRLB until the SNR is sufficient to guarantee that the estimate is localized to within the correct carrier cycle. At low SNR, the magnitude estimators are not sufficiently accurate, so the phase refinement cannot disambiguate the phase information and can mistake adjacent carrier cycles for the true value. In the low SNR regime, this estimator is dominated by these cycle slips. The phase refinement estimator with carrier synthesizer resets (blue/diamond) does perform significantly better than the interpolator at high SNR, but requires higher SNR to make the transition and plateaus at about 1 mm standard deviation. The plateau of the purple curve is caused by insufficient resolution in the simulation platform.

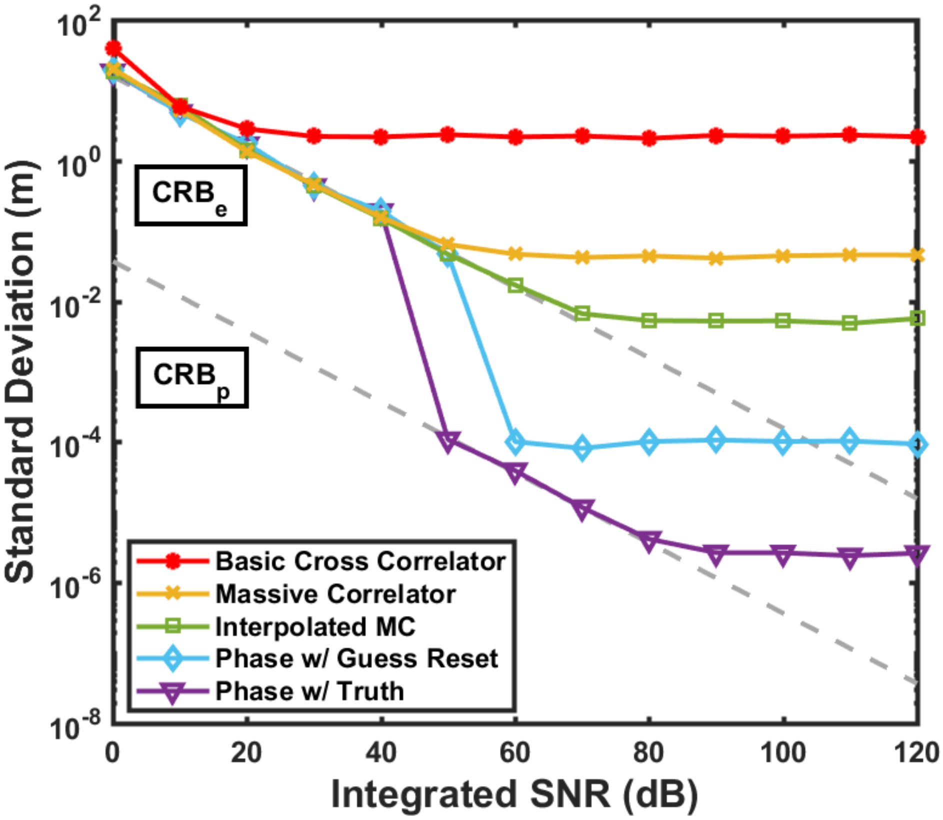

Figure 4.2: Monte Carlo simulation results. Five estimation techniques are compared for a range of integrated SNRs. The three magnitude estimators (red, yellow, green) are bounded by the CRLB in (4.19). The phase refinement estimators (blue, purple) are bounded by the CRLB in (4.22), but do not reach this bound until the integrated SNR is sufficient to avoid cycle slips. In the low SNR regime, the phase recovery estimators may lock on to ambiguities across carrier cycles. These 2 estimators are only asymptotically unbiased as the probability of cycle slips is driven to zero. The bottom curve plateaus as it reaches the resolution of the simulation environment.

Chapter 5

TIME-OF-FLIGHT ESTIMATION

We design a network exchange algorithm that estimates and tracks the distance between users and synchronizes the distributed clock sources. This algorithm is inspired by the Network Timing Protocol (NTP) in which users exchange time information to synchronize their clocks. We design an algorithm labeled HTP that tracks the state space variables across exchanges between users and extracts time-of-flight estimates between each antenna pair.

5.1 Network Timing Protocol

The HTP algorithm is broken into 2 stages: an acquisition stage, and a tracking stage. The acquisition stage closely resembles the Network Timing Protocol. During this stage, two radios alternate transmitting and receiving data. When radio B receives a message, it estimates when that message arrived ($t_{B,Rx}^{(n)}$) and when it will transmit the next one ($t_{B,Tx}^{(n+1)}$). These two timestamps are included in the next transmission such that radio A has access to these values.

After a transmission cycle A → B → A, radio A estimates the time of flight τ and time offset T for each of the two frames. Index these two frames by n and $n-1$, as depicted in Figure 5.1. For the transmission A → B, the received timestamp is modeled as

$$t_{B,Rx}^{(n-1)} = t_{A,Tx}^{(n-1)} + \tau^{(n-1)} - T^{(n-1)}. \tag{5.1}$$

For the transmission B → A, the received timestamp is modeled as

$$t_{A,Rx}^{(n)} = t_{B,Tx}^{(n)} + \tau^{(n)} + T^{(n)}. \tag{5.2}$$

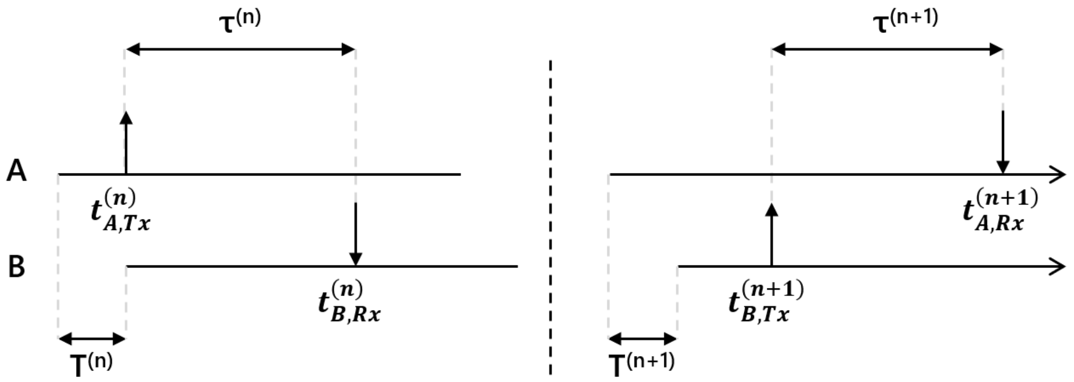

Figure 5.1: Transmission cycle from A → B → A. The variables necessary to execute the acquisition stage of the algorithm are labeled.

We leverage the difference in the sign of $T^{(n-1)}$ and $T^{(n)}$ to estimate the state space variables. This stage in the protocol makes the following assumptions:

1. Both radios have been registered on the network.
2. Both radios have agreed to cooperate and have defined a frame length l.
3. Master and slave nodes have been assigned.
4. The time offset T does not change significantly from frame $n-1$ to frame n, i.e. $T^{(n-1)} = T^{(n)}$.
5. The time delay τ does not change significantly from frame $n-1$ to frame n, i.e. $\tau^{(n-1)} = \tau^{(n)}$.

When a radio receives a transmission, it decodes the timestamp information embedded in the message. With these timestamps and assumptions 4 and 5, Equations (5.1) and (5.2) become a system of 2 linear equations with 2 unknowns. Each radio solves this system as follows.

Algorithm:

A: $\forall n \in [2, 4, 6, ...]$,

1. Compute $\hat{\gamma}_A^{(n)}$ using:

$$\hat{\gamma}_A^{(n)} = (\hat{t}_{A,Rx}^{(n)} - t_{A,Tx}^{(n-1)}) - (t_{B,Tx}^{(n)} - \hat{t}_{B,Rx}^{(n-1)}) \tag{5.3}$$

2. Estimate $\tau^{(n)}$ and $\tau^{(n-1)}$ using assumption 5 and (5.3):

$$\hat{\tau}^{(n)} = \frac{\hat{\gamma}_A^{(n)}}{2} \tag{5.4}$$

$$\hat{\tau}^{(n-1)} = \frac{\hat{\gamma}_A^{(n)}}{2} \tag{5.5}$$

3. Estimate $T^{(n)}$ and $T^{(n-1)}$ using Equations (5.1) and (5.2):

$$\hat{T}^{(n)} = \hat{t}_{A,Rx}^{(n)} - t_{B,Tx}^{(n)} - \hat{\tau}^{(n)} \tag{5.6}$$

$$\hat{T}^{(n-1)} = t_{A,Tx}^{(n-1)} - \hat{t}_{B,Rx}^{(n-1)} + \hat{\tau}^{(n-1)} \tag{5.7}$$

4. If $n > 2$, track the first order derivatives. Let M be the total number of iterations performed, such that $\hat{l}_A^{(n-2,M)}$ is the frame length estimate of the last iteration of the previous processing cycle. For the current cycle use the nominal value of l_A.

$$\dot{\hat{\tau}}^{(n)} = \frac{\hat{\tau}^{(n)} - \hat{\tau}^{(n-2)}}{l_A^{(n-1)} + \hat{l}_A^{(n-2,M)}} \tag{5.8}$$

$$\dot{\hat{\tau}}^{(n-1)} = \dot{\hat{\tau}}^{(n)} \tag{5.9}$$

$$\dot{\hat{T}}^{(n)} = \frac{\hat{T}^{(n)} - \hat{T}^{(n-2)}}{l_A^{(n-1)} + \hat{l}_A^{(n-2,M)}} \tag{5.10}$$

$$\dot{\hat{T}}^{(n-1)} = \dot{\hat{T}}^{(n)} \tag{5.11}$$

Algorithm:

B: $\forall n \in [3, 5, 7, ...]$,

1. Compute $\hat{\gamma}_B^{(n)}$ using:

$$\hat{\gamma}_B^{(n)} = (\hat{t}_{B,Rx}^{(n)} - t_{B,Tx}^{(n-1)}) - (t_{A,Tx}^{(n)} - \hat{t}_{A,Rx}^{(n-1)}) \tag{5.12}$$

2. Estimate $\tau^{(n)}$ and $\tau^{(n-1)}$ using assumption 5 and (5.12):

$$\hat{\tau}^{(n)} = \frac{\hat{\gamma}_B^{(n)}}{2} \tag{5.13}$$

$$\hat{\tau}^{(n-1)} = \frac{\hat{\gamma}_B^{(n)}}{2} \tag{5.14}$$

3. Estimate $T^{(n)}$ and $T^{(n-1)}$ using Equations (5.2) and (5.1):

$$\hat{T}^{(n)} = t_{A,Tx}^{(n)} - \hat{t}_{B,Rx}^{(n)} + \hat{\tau}^{(n)} \tag{5.15}$$

$$\hat{T}^{(n-1)} = \hat{t}_{A,Rx}^{(n-1)} - t_{B,Tx}^{(n-1)} - \hat{\tau}^{(n-1)} \tag{5.16}$$

4. If $n > 3$, track the first order derivatives. Let M be the total number of iterations performed, such that $\hat{l}_B^{(n-2,M)}$ is the frame length estimate of the last iteration of the previous processing cycle. For the current cycle use the nominal value of l_B.

$$\hat{\dot{\tau}}^{(n)} = \frac{\hat{\tau}^{(n)} - \hat{\tau}^{(n-2)}}{l_B^{(n-1)} + \hat{l}_B^{(n-2,M)}} \tag{5.17}$$

$$\hat{\dot{\tau}}^{(n-1)} = \hat{\dot{\tau}}^{(n)} \tag{5.18}$$

$$\hat{\dot{T}}^{(n)} = \frac{\hat{T}^{(n)} - \hat{T}^{(n-2)}}{l_B^{(n-1)} + \hat{l}_B^{(n-2,M)}} \tag{5.19}$$

$$\hat{\dot{T}}^{(n-1)} = \hat{\dot{T}}^{(n)} \tag{5.20}$$

This acquisition stage requires few calculations and is easy to implement, but has the following limitations:

1. τ is assumed to be constant between each frame. This is not a good assumption for moving targets.
2. T is assumed to be constant between each frame. This is not a good assumption for poorly behaved oscillators.
3. Transmission timestamps are assumed to be known perfectly. This is not a good assumption without careful calibration of the transmitters.
4. The frame length l is assumed to be known and constant. For clocks with significant drift or misalignment, this is not a good assumption.
5. Estimates of the state space occur only every other frame.

These limitations are addressed in the tracking stage.

5.2 Synchronization Preliminaries

We relax some of the assumptions made in the acquisition stage of the synchronization algorithm and adjust the estimators accordingly. The tracking stage iteratively refines state space estimates, indexed by k.

5.2.1 Velocity Compensation

Relax the assumption that $\tau^{(n-1)} = \tau^{(n)}$. Leverage previous estimates of $\dot{\tau}$ to perform a weighted division of γ instead of simply dividing by 2. Using the $\dot{\tau}^{(n)}$ estimate for the $k-1$ frame, adjust the estimates for $\tau^{(n-1)}$ and $\tau^{(n)}$ as follows:

$$\begin{aligned}
\hat{\gamma}_A^{(n)} &= (\hat{t}_{A,Rx}^{(n)} - t_{A,Tx}^{(n-1)}) - (t_{B,Tx}^{(n)} - \hat{t}_{B,Rx}^{(n-1)}) \\
&\approx \hat{\tau}^{(k,n-1)} + \hat{\tau}^{(k,n)} \\
&\approx \hat{\tau}^{(k,n-1)} + \left(\hat{\tau}^{(k,n-1)} + \hat{\dot{\tau}}^{(k-1,n-1)} l^{(k,n-1)}\right) \\
&= 2\hat{\tau}^{(k,n-1)} + \hat{\dot{\tau}}^{(k-1,n-1)} l^{(k,n-1)} \\
\rightarrow \hat{\tau}^{(k,n-1)} &= \frac{\hat{\gamma}_A^{(n)} - \hat{\dot{\tau}}^{(k-1,n-1)} l_A^{(k,n-1)}}{2} && (5.21) \\
\rightarrow \hat{\tau}^{(k,n)} &= \hat{\gamma}_A^{(n)} - \hat{\tau}^{(k,n-1)} && (5.22) \\
&= \frac{\hat{\gamma}_A^{(n)} + \hat{\dot{\tau}}^{(k-1,n-1)} l_A^{(k,n-1)}}{2} && (5.23)
\end{aligned}$$

The same process may be applied to the processing chain at radio B:

$$\begin{aligned}
\hat{\gamma}_B^{(n)} &= (\hat{t}_{B,Rx}^{(n)} - t_{B,Tx}^{(n-1)}) - (t_{A,Tx}^{(n)} - \hat{t}_{A,Rx}^{(n-1)}) \\
\rightarrow \hat{\tau}^{(k,n-1)} &= \frac{\gamma_B^{(n)} - \hat{\dot{\tau}}^{(k-1,n-1)} l^{(k,n-1)}}{2} && (5.24) \\
\rightarrow \hat{\tau}^{(k,n)} &= \hat{\gamma}_B^{(n)} - \hat{\tau}^{(k,n-1)} && (5.25) \\
&= \frac{\gamma_B^{(n)} + \hat{\dot{\tau}}^{(k-1,n-1)} l^{(k,n-1)}}{2} && (5.26)
\end{aligned}$$

5.2.2 Frequency Compensation

Relax the assumption that $T^{(n-1)} = T^{(n)}$. Perform a similar adjustment to the division of γ as the velocity compensation:

$$\begin{aligned}
\hat{\gamma}_A^{(n)} &= (\hat{t}_{A,Rx}^{(n)} - t_{A,Tx}^{(n-1)}) - (t_{B,Tx}^{(n)} - \hat{t}_{B,Rx}^{(n-1)}) \\
&\approx \hat{\tau}^{(k,n-1)} - \hat{T}^{(k,n-1)} + \hat{\tau}^{(k,n)} + \hat{T}^{(k,n)} \\
&\approx \hat{\tau}^{(k,n-1)} + \left(\hat{\tau}^{(k,n-1)} + \hat{\dot{\tau}}^{(k-1,n-1)} l^{(k,n-1)}\right) - \hat{T}^{(k,n-1)} + \left(\hat{T}^{(k,n-1)} + \hat{\dot{T}}^{(k-1,n-1)} l^{(k,n-1)}\right) \\
&= 2\hat{\tau}^{(k,n-1)} + \hat{\dot{\tau}}^{(k-1,n-1)} l^{(k,n-1)} + \hat{\dot{T}}^{(k-1,n-1)} l^{(k,n-1)} \\
\rightarrow \hat{\tau}^{(k,n-1)} &= \frac{\gamma_A^{(n)} - \hat{\dot{\tau}}^{(k-1,n-1)} \hat{l}_A^{(k,n-1)} - \hat{\dot{T}}^{(k-1,n-1)} \hat{l}_A^{(k,n-1)}}{2} && (5.27) \\
\rightarrow \hat{\tau}^{(k,n)} &= \frac{\gamma_A^{(n)} + \hat{\dot{\tau}}^{(k-1,n-1)} \hat{l}_A^{(k,n-1)} - \hat{\dot{T}}^{(k-1,n-1)} \hat{l}_A^{(k,n-1)}}{2} && (5.28)
\end{aligned}$$

The same process may be applied to the processing chain at radio B:

$$\begin{aligned}
\gamma_B^{(n)} &= (\hat{t}_{B,Rx}^{(n)} - t_{B,Tx}^{(n-1)}) - (t_{A,Tx}^{(n)} - \hat{t}_{A,Rx}^{(n-1)}) \\
\rightarrow \hat{\tau}^{(k,n-1)} &= \frac{\gamma_B^{(n)} - \hat{\dot{\tau}}^{(k-1,n-1)} \hat{l}_B^{(k,n-1)} + \hat{\dot{T}}^{(k-1,n-1)} \hat{l}_B^{(k,n-1)}}{2} && (5.29) \\
\rightarrow \hat{\tau}^{(k,n)} &= \frac{\gamma_B^{(n)} + \hat{\dot{\tau}}^{(k-1,n-1)} \hat{l}_B^{(k,n-1)} + \hat{\dot{T}}^{(k-1,n-1)} \hat{l}_B^{(k,n-1)}}{2} && (5.30)
\end{aligned}$$

5.2.3 Frame Length Refinement

Relax the assumption that the frame length l is known perfectly and is a constant value. If the frame length changes between each frame, computing the derivatives using every other frame is less accurate. Instead of using the nominal value, estimate the frame length by estimating the difference in adjacent transmission times for each frame. This requires a time conversion of one the transmit timestamps, shown in Figure 5.2 as $\tilde{t}_{A,Tx}^{(n+1)}$. This represents the time at which the transmit event $t_{B,Tx}^{(n+1)}$ occurred as perceived by radio A. The frame lengths $l^{(n)}$ and $l^{(n-1)}$ are then defined as

$$l^{(n-1)} = \tilde{t}_{A,Tx}^{(n)} - t_{A,Tx}^{(n-1)} \tag{5.31}$$

$$l^{(n-2)} = t_{A,Tx}^{(n-1)} - \tilde{t}_{A,Tx}^{(n-2)} \tag{5.32}$$

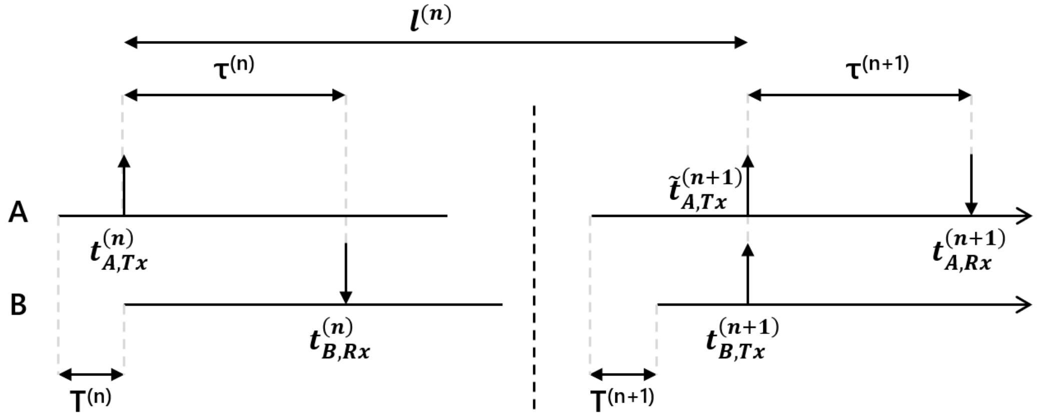

Figure 5.2: Timing diagram depicting the conversion of a transmit event to estimate the frame length.

Carefully compute this conversion as:

$$\begin{aligned}
\tilde{t}^{(k,n)}_{A,Tx} &= t^{(n)}_{B,Tx} + T^{(n)} \\
&\approx t^{(n)}_{B,Tx} + (\hat{T}^{(k-1,n-1)} + \dot{\hat{T}}^{(k-1,n-1)}(\tilde{t}^{(k,n)}_{A,Tx} - t^{(n-1)}_{A,Tx})) \\
&= t^{(n)}_{B,Tx} + \hat{T}^{(k-1,n-1)} + \dot{\hat{T}}^{(k-1,n-1)}\tilde{t}^{(k,n)}_{A,Tx} - \dot{\hat{T}}^{(k-1,n-1)}t^{(n-1)}_{A,Tx} \\
&= \frac{t^{(n)}_{B,Tx} + \hat{T}^{(k-1,n-1)} - \dot{\hat{T}}^{(k-1,n-1)}t^{(n-1)}_{A,Tx}}{1 - \dot{\hat{T}}^{(k-1,n-1)}} \quad n = [2,4,6,...] \qquad (5.33) \\
\tilde{t}^{(k,n)}_{B,Tx} &= \frac{t^{(n)}_{A,Tx} - \hat{T}^{(k-1,n-1)} + \dot{\hat{T}}^{(k-1,n-1)}t^{(n-1)}_{B,Tx}}{1 + \dot{\hat{T}}^{(k-1,n-1)}} \quad n = [3,5,7,...] \qquad (5.34)
\end{aligned}$$

5.3 Herschfelt Timing Protocol

The complete HTP dynamically transitions between the acquisition and tracking stages as appropriate. The acquisition stage is the adaptation of the NTP defined above. The tracking stage iteratively refines the state space estimates with the velocity, frequency, and frame length compensations defined above. Which of these refinements are performed, the order in which they are performed, and how many iterations are performed in each are design parameters of the HTP.

The first iteration in every frame is the adapted NTP computations. If the system is idling in the acquisition stage, this the only iteration performed for that frame. If the system has transitioned to the tracking stage, additional iterations are performed to refine the estimates. Each refinement is assigned a number of iterations. When all iterations for that refinement are complete, the next refinement is performed. Refinements are performed in the following order: velocity compensation, frequency compensation, and frame length refinement. The computations performed in each sub-stage are defined below.

5.3.1 Velocity Compensation Equations (A)

Let K_1 be the number of iterations for this sub-stage.

1. Perform the acquisition stage to generate initial estimates ($k = 0$):

$$\left[\hat{\tau}^{(0,n-1)}, \hat{\tau}^{(0,n)}, \hat{T}^{(0,n-1)}, \hat{T}^{(0,n)}, \hat{\dot{\tau}}^{(0,n-1)}, \hat{\dot{\tau}}^{(0,n)}, \hat{\dot{T}}^{(0,n-1)}, \hat{\dot{T}}^{(0,n)}\right]$$

2. Compute $\hat{\gamma}_A^{(n)}$ using (5.3).

3. For $k = 1 : K_1$ iterations...

   (a) Compute $\hat{\tau}^{(k,n-1)}$ and $\hat{\tau}^{(k,n)}$ using (5.21) and (5.23).

   (b) Compute $\hat{T}^{(k,n-1)}$ and $\hat{T}^{(k,n)}$ using

$$\hat{T}^{(k,n-1)} = t_{A,Tx}^{(n-1)} - \hat{t}_{B,Rx}^{(n-1)} + \hat{\tau}^{(k,n-1)} \tag{5.35}$$

$$\hat{T}^{(k,n)} = \hat{t}_{A,Rx}^{(n)} - t_{B,Tx}^{(n)} - \hat{\tau}^{(k,n)} \tag{5.36}$$

   (c) Import previous $\dot{T}$ values computed using (5.10) and (5.11):

$$\hat{\dot{T}}^{(k,n)} = \hat{\dot{T}}^{(0,n)}$$

$$\hat{\dot{T}}^{(k,n-1)} = \hat{\dot{T}}^{(0,n-1)}$$

   (d) If the protocol transitioned to tracking during this frame:

$$\hat{\dot{\tau}}^{(k,n)} = \hat{\dot{\tau}}^{(0,n)}$$

$$\hat{\dot{\tau}}^{(k,n-1)} = \hat{\dot{\tau}}^{(0,n-1)}$$

   (e) Else, compute $\hat{\dot{\tau}}^{(k,n-1)}$ and $\hat{\dot{\tau}}^{(k,n)}$ using

$$\hat{\dot{\tau}}^{(k,n)} = \frac{\hat{\tau}^{(k,n)} - \hat{\tau}^{(k,n-2)}}{l^{(n-1)} + l^{(n-2)}} \tag{5.37}$$

$$\hat{\dot{\tau}}^{(k,n-1)} = \hat{\dot{\tau}}^{(k,n)} \tag{5.38}$$

5.3.2 Velocity Compensation Equations (B)

Let K_1 be the number of iterations for this sub-stage.

1. Perform the acquisition stage to generate initial estimates ($k = 0$):

$$\left[\hat{\tau}^{(0,n-1)}, \hat{\tau}^{(0,n)}, \hat{T}^{(0,n-1)}, \hat{T}^{(0,n)}, \hat{\dot{\tau}}^{(0,n-1)}, \hat{\dot{\tau}}^{(0,n)}, \hat{\dot{T}}^{(0,n-1)}, \hat{\dot{T}}^{(0,n)}\right]$$

2. Compute $\hat{\gamma}_B^{(n)}$ using (5.12).

3. For $k = 1 : K_1$ iterations...

   (a) Compute $\hat{\tau}^{(k,n-1)}$ and $\hat{\tau}^{(k,n)}$ using (5.24) and (5.26).

   (b) Compute $\hat{T}^{(k,n-1)}$ and $\hat{T}^{(k,n)}$ using

$$\hat{T}^{(k,n-1)} = \hat{t}_{A,Rx}^{(n-1)} - t_{B,Tx}^{(n-1)} - \hat{\tau}^{(k,n-1)} \tag{5.39}$$

$$\hat{T}^{(k,n)} = t_{A,Tx}^{(n)} - \hat{t}_{B,Rx}^{(n)} + \hat{\tau}^{(k,n)} \tag{5.40}$$

   (c) Import previous $\dot{T}$ values computed using (5.19) and (5.20):

$$\hat{\dot{T}}^{(k,n)} = \hat{\dot{T}}^{(0,n)} \tag{5.41}$$

$$\hat{\dot{T}}^{(k,n-1)} = \hat{\dot{T}}^{(0,n-1)} \tag{5.42}$$

   (d) If the protocol transitioned to tracking during this frame:

$$\hat{\dot{\tau}}^{(k,n)} = \hat{\dot{\tau}}^{(0,n)} \tag{5.43}$$

$$\hat{\dot{\tau}}^{(k,n-1)} = \hat{\dot{\tau}}^{(0,n-1)} \tag{5.44}$$

   (e) Else, compute $\hat{\dot{\tau}}^{(k,n-1)}$ and $\hat{\dot{\tau}}^{(k,n)}$ using

$$\hat{\dot{\tau}}^{(k,n)} = \frac{\hat{\tau}^{(k,n)} - \hat{\tau}^{(k,n-2)}}{l^{(n-1)} + l^{(n-2)}} \tag{5.45}$$

$$\hat{\dot{\tau}}^{(k,n-1)} = \hat{\dot{\tau}}^{(k,n)} \tag{5.46}$$

5.3.3 Frequency Compensation Equations (A)

Let K_2 be the number of iterations for this sub-stage.

1. Perform the first K_1 iterations of velocity compensation.

2. Compute $\hat{\gamma}_A^{(n)}$ using (5.3).

3. For $k = (K_1 + 1) : (K_1 + 1 + K_2)$ iterations...

   (a) Compute $\hat{\tau}^{(k,n-1)}$ and $\hat{\tau}^{(k,n)}$ using (5.27) and (5.28).

   (b) Compute $\hat{T}^{(k,n-1)}$ and $\hat{T}^{(k,n)}$ using (5.35) and (5.36).

   (c) Import previous $\dot{T}$ values computed using (5.10) and (5.11):

$$\begin{aligned} \hat{\dot{T}}^{(k,n)} &= \hat{\dot{T}}^{(0,n)} \\ \hat{\dot{T}}^{(k,n-1)} &= \hat{\dot{T}}^{(0,n-1)} \end{aligned}$$

   (d) If the protocol transitioned to tracking during this frame:

$$\begin{aligned} \hat{\dot{\tau}}^{(k,n)} &= \hat{\dot{\tau}}^{(0,n)} \\ \hat{\dot{\tau}}^{(k,n-1)} &= \hat{\dot{\tau}}^{(0,n-1)} \end{aligned}$$

   (e) Else, compute $\hat{\dot{\tau}}^{(k,n-1)}$ and $\hat{\dot{\tau}}^{(k,n)}$ using

$$\hat{\dot{\tau}}^{(k,n)} = \frac{\hat{\tau}^{(k,n)} - \hat{\tau}^{(k,n-2)}}{l^{(n-1)} + l^{(n-2)}} \tag{5.47}$$

$$\hat{\dot{\tau}}^{(k,n-1)} = \frac{\hat{\tau}^{(k,n-1)} - \hat{\tau}^{(k,n-3)}}{l^{(n-2)} + l^{(n-3)}} \tag{5.48}$$

5.3.4 Frequency Compensation Equations (B)

Let K_2 be the number of iterations for this sub-stage.

1. Perform the first K_1 iterations of velocity compensation.

2. Compute $\hat{\gamma}_B^{(n)}$ using (5.12).

3. For $k = (K_1 + 1) : (K_1 + 1 + K_2)$ iterations...

   (a) Compute $\hat{\tau}^{(k,n-1)}$ and $\hat{\tau}^{(k,n)}$ using (5.29) and (5.30).

   (b) Compute $\hat{T}^{(k,n-1)}$ and $\hat{T}^{(k,n)}$ using (5.39) and (5.40).

   (c) Import previous $\dot{T}$ values computed using (5.10) and (5.11):

   $$\hat{\dot{T}}^{(k,n)} = \hat{\dot{T}}^{(0,n)}$$
   $$\hat{\dot{T}}^{(k,n-1)} = \hat{\dot{T}}^{(0,n-1)}$$

   (d) If the protocol transitioned to tracking during this frame:

   $$\hat{\dot{\tau}}^{(k,n)} = \hat{\dot{\tau}}^{(0,n)}$$
   $$\hat{\dot{\tau}}^{(k,n-1)} = \hat{\dot{\tau}}^{(0,n-1)}$$

   (e) Else, compute $\dot{\hat{\tau}}^{(k,n-1)}$ and $\dot{\hat{\tau}}^{(k,n)}$ using

   $$\hat{\dot{\tau}}^{(k,n)} = \frac{\hat{\tau}^{(k,n)} - \hat{\tau}^{(k,n-2)}}{l^{(n-1)} + l^{(n-2)}} \tag{5.49}$$
   $$\hat{\dot{\tau}}^{(k,n-1)} = \frac{\hat{\tau}^{(k,n-1)} - \hat{\tau}^{(k,n-3)}}{l^{(n-2)} + l^{(n-3)}} \tag{5.50}$$

Chapter 6

EXPERIMENTAL RESULTS

The time-of-arrival (ToA) estimation techniques and time-of-flight (ToF) algorithm were implemented on experimental hardware testbeds by several graduate students in the Bliss Laboratory of Information, Signals, and Systems. The following chapter details several experimental results using these test platforms. These results represent the culmination of significant effort from all indivduals who worked on this program; I present them not as my own contribution, but as context and validation of the methods described in the previous chapters.

6.1 Cabled Tests

The first set of experimental tests consists of two experimental testbeds operating with independent clock sources connected via RF cables and an RF combiner. These tests verify the functionality of the proposed ToA estimators and ToF algorithm. The current iteration of the hardware operates using the interpolated massive correlator ToA estimator; the phase refinement estimator is still being developed on the hardware. For the following experiments, the platforms maintain an integrated SNR of about 60 dB.

The two platforms are connected via RF cables, so the following tests isolate the performance of the estimators in a stable, stationary environment. These platforms execute the joint positioning-communications system described in Chapter 2, alternating transmitting and receiving the joint waveform. Each user estimates the ToA of each positioning sequence on each receive channel, runs the ToF synchronization algorithm, and shares the informaiton with the other user in the next transmission.

For the first set of data, the platforms execute the massive correlator ToA estimator without interpolation. The resulting ToF estimates using HTP are depicted in Figure 6.1. I plot the resulting ToF estimates for a single channel, and subtract the mean to emphasize the variance around what should be a stable estimate. The quantization due to the resolution of the massive correlator is clearly visible in the ToF estimates. The resulting variance is 5.5 cm, which is consistent with the simulation results depicted in Figure 4.2.

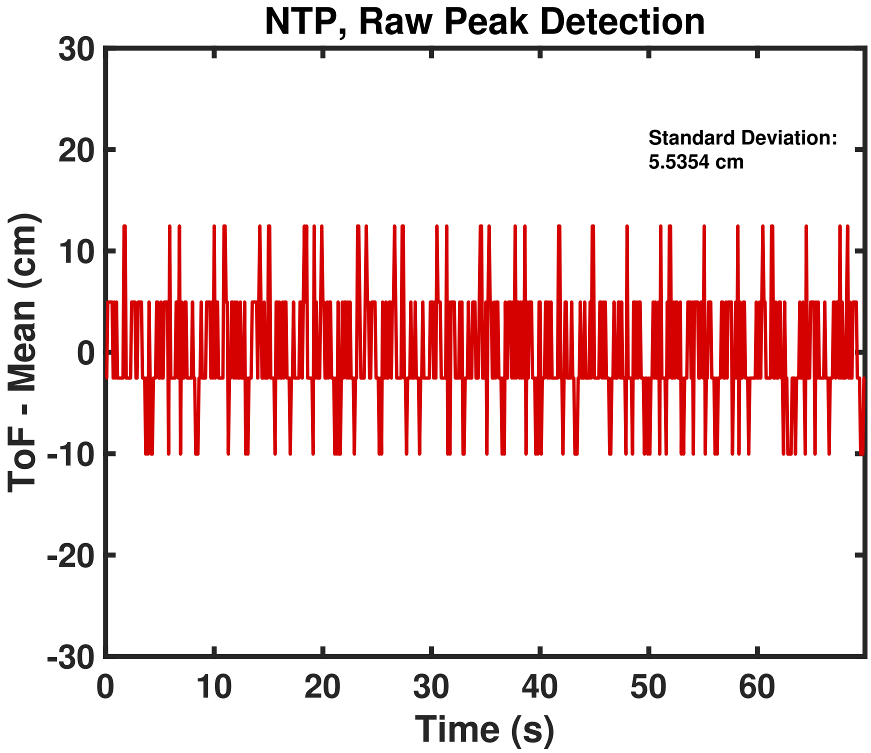

Figure 6.1: Experimental data set processed using the massive correlation ToA estimator without interpolation. ToF is computed using the HTP algorithm. The mean is subtracted to emphasize the variation in the estimates. The standard deviation for this data set is 5.5 cm.

For the next data set, the platforms additionally compute the interpolated peak of the massive correlator output to refine the ToA estimate. The results depicted in Figure 6.2 demonstrate the performance improvement for an identical experimental setup. The resulting standard deviation is 1.6 cm, which is also consistent with the simulated results. Please note that the ToF estimates are functions of the ToA estimates, so the standard deviations reported on ToA in Figure 4.2 must be transformed according to the functions in the ToF algorithm to represent standard deviations on ToF. For the full HTP algorithm, this process is cumbersome, but for the basic NTP algorithm the variance is simply doubled, thus the standard deviation of ToF vs ToA is simply multipled by $\sqrt{2}$.

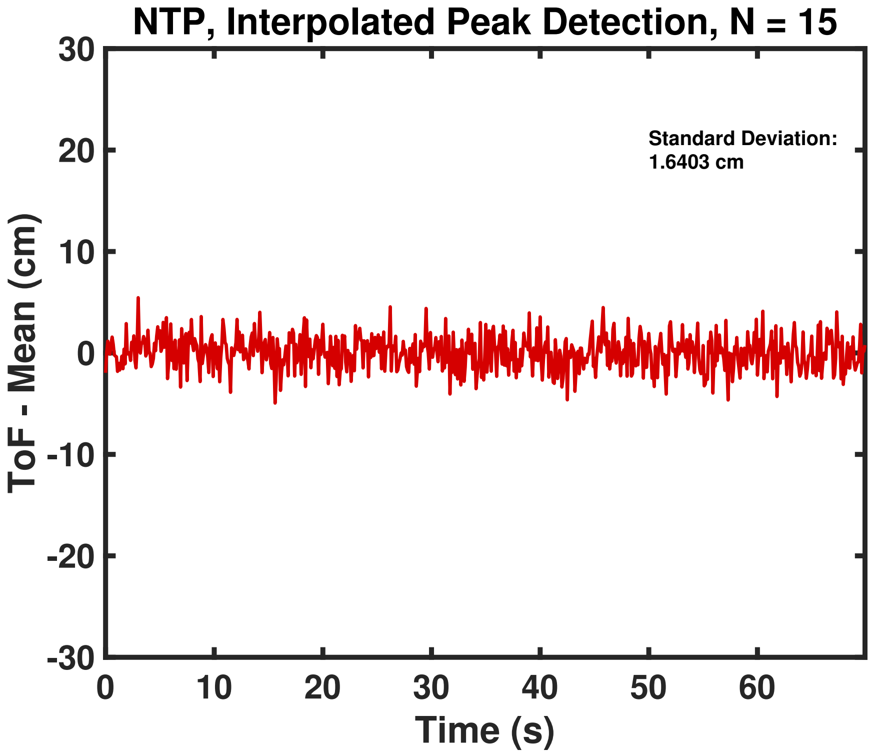

Figure 6.2: Second experimental data set, collected with an identical setup to the results in Figure 6.1, but additionally processed using the interpolated ToA estimator.

We then compared the ToF standard deviation for different choices of the number of samples N used in the ToA interpolation. The results are displayed in Figure 6.3. For this experimental setup, it is trivial to post-process this data with different choices of N, but in an actual system N must be chosen ahead of time. These results therefore allow us to make an informed decision on the number of samples used in the interpolation. The figure below indicates that any number of samples greater than $N = 11$ offers diminishing returns in terms of ToF performance.

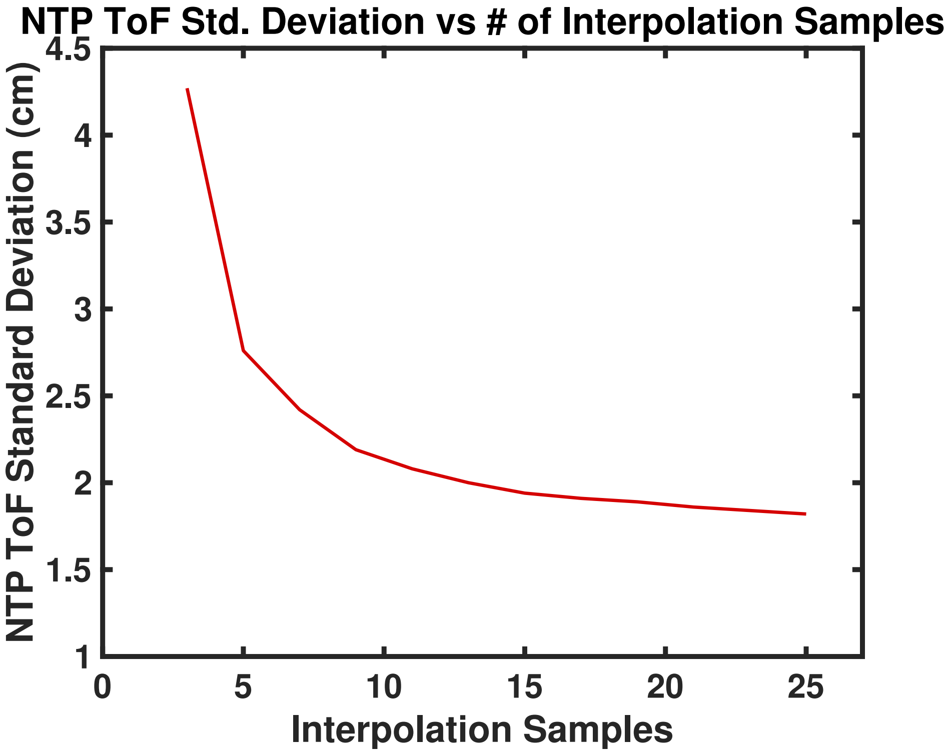

Figure 6.3: ToF estimation standard deviation as a function of the number of correlation samples N used to estimate the interpolation of the massive correlator.

6.1.1 Kalman Filter Performance

Kalman filters may be applied to these data sets to reduce the standard deviation of the ToF estimates. The previous data sets are run through a first order extended Kalman filter with adaptive Q estimation every iteration. We compare the interpolated peak detection performance using different initial Q estimates. The results for three different initial estimates are presented in Figure 6.4. These results significantly outperform the previous estimators, offering a standard deviation as low as 3.1 mm for certain choices of Q. However, the Kalman filter requires some time to settle, as seen in the first part of the plat, and is sensitive to the initial choices in seting up the filter.

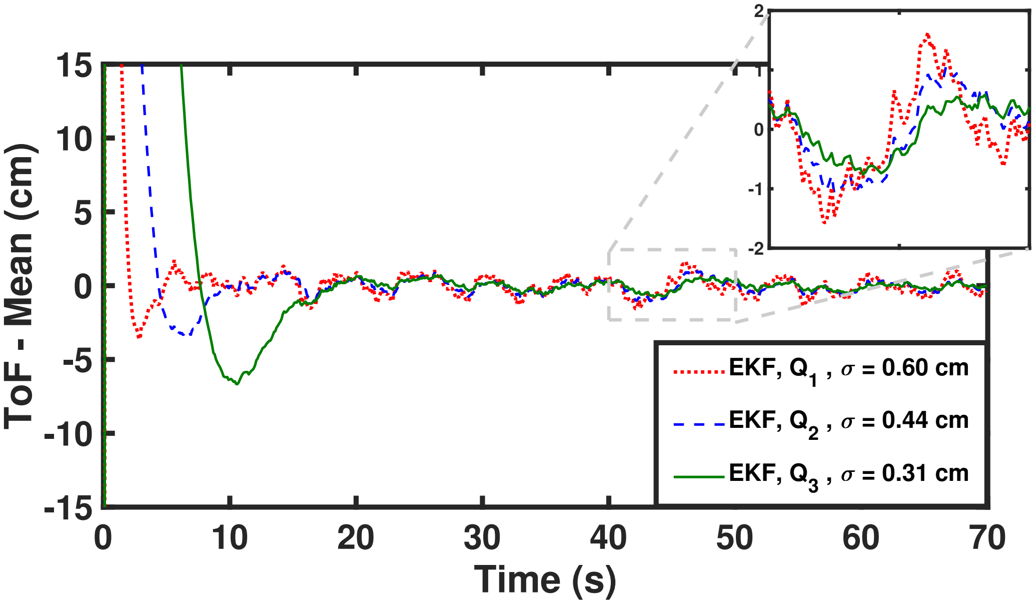

Figure 6.4: Performance comparison of three Kalman filters with different initial Q estimates. The Kalman filter significantly outperforms the basic ToA estimators, but requires time to settle on a solution.

6.2 Flight Tests

As a team,we performed five flight tests at the general aviation airport in Nördlingen, Germany. These flight tests included two experimental platforms, one installed in a box and connected to 4 telescoping antennas, and another mounted to a UAS. These are depicted in Figure 6.5. We installed the base-station at one end of the runway and designated a launch point for the UAV on the runway and normalized the coordinate system such that this point resides at (0,0). These flight tests were performed earlier in the program before the interpolated ToA estimator had been fully implemented, so the following results are computed using the massive correlation ToA estimator.

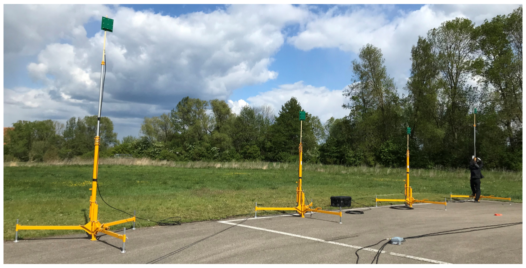

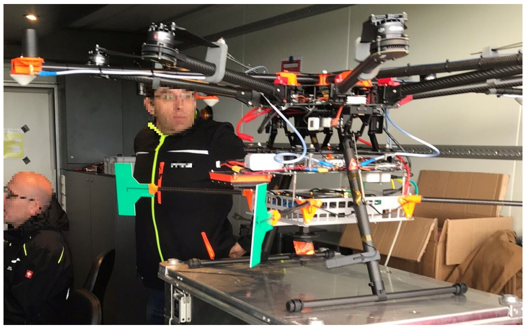

Figure 6.5: Experimental testbeds for the flight tests in Nördlingen, Germany. The base-station (left) consists of 4 antennas moutnmed on telescoping platforms. The hardware is mounted in the black box in the center of the picture. The UAS (right) is a DJI S1000+ UAV equipped with the hardware mounted in an aluminum frame and a tachymeter reference.

6.2.1 Engine Test

The first test investigated the effects of the UAV engines on the system. The system was activated and calibrated, then the engines were turned on and off while the system was running. The range estimates from the base-station to one of the UAV antennas are displayed in Figure 6.6. The estimates are reasonably stable, indicating that the engines have little to no effect on the range estimates.

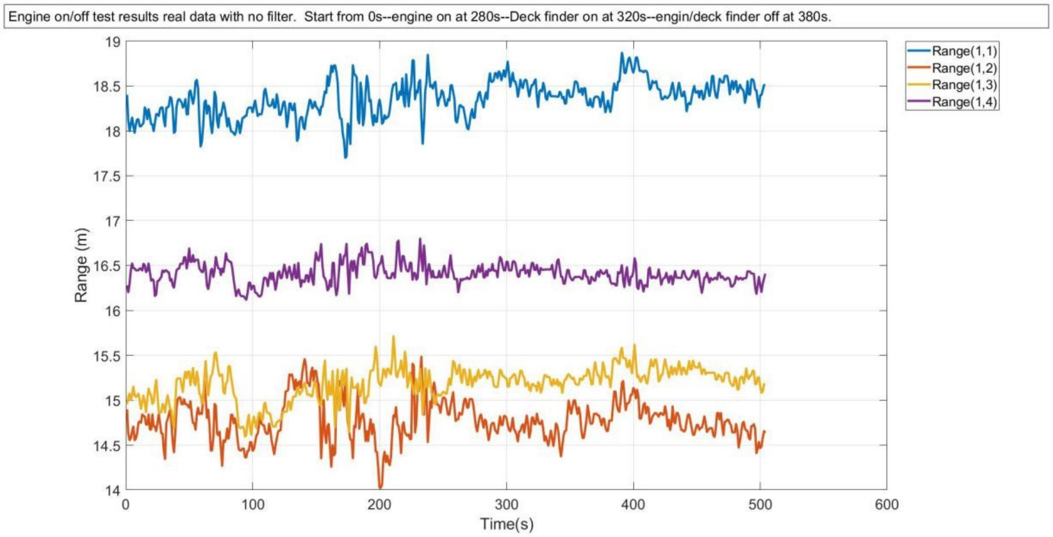

Figure 6.6: Range estimates for drone antenna 1 to base-station antennas 1-4 produced during the engine test. The estimates are reasonably stable, indicating that the engines have little to no effect on the range estimates.

6.2.2 VTOL Test

The second test was a close-range test in which the UAV was positioned on the ground about 13 meters away from the base-station. While the system was running, two operators picked up the UAV and walked towards the base-station, then returned it to its original location. We then turned on the UAV and performed a vertical take-off and landing (VTOL) test in which the drone ascended several meters, hovered, then returned to the ground. The resulting range estimates for one of the antenna pairs are depicted in Figure 6.7, plotted against a tachymeter reference. There is a slight bias throughout the data due to the different positions of the tachymeter and reference antenna on the UAV. The ranging performance degrades dramatically when the operators shielded the line-of-sight path to the antenna, but when this link is restored the range estimates closely follow the tachymeter reference. The variation during the hovering stage was caused by the high winds experienced throughout the day.

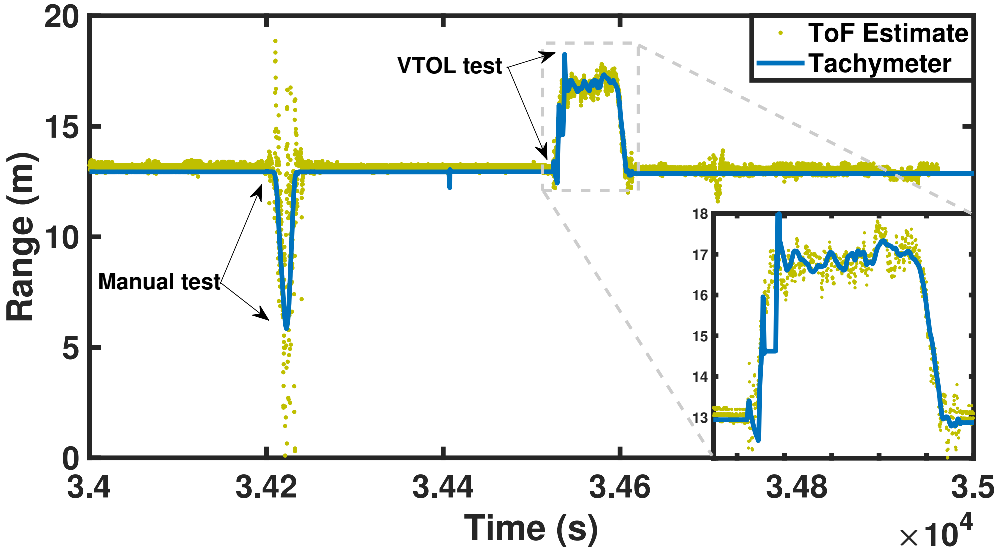

Figure 6.7: Range estimation results for the manual relocation and vertical take off and landing tests. During the manual test, the operators picking up the UAV obstruct the line-of-sight path between the base station and UAV, which significantly degrades the system performance. During the VTOL test, the range estimation closely follows the tachymeter reference.

6.2.3 Short Range Test

The third test investigated the system's ability to maintain a given ranging precision as the UAV moved away from the base-station. We flew the UAV in a straight line down the runway for about 750 meters, let it hover, then landed it at the other end of the runway. The resulting range estimates are displayed in Figure 6.8, which indicate the system was able to maintain its ranging precision for the duration of the flight.

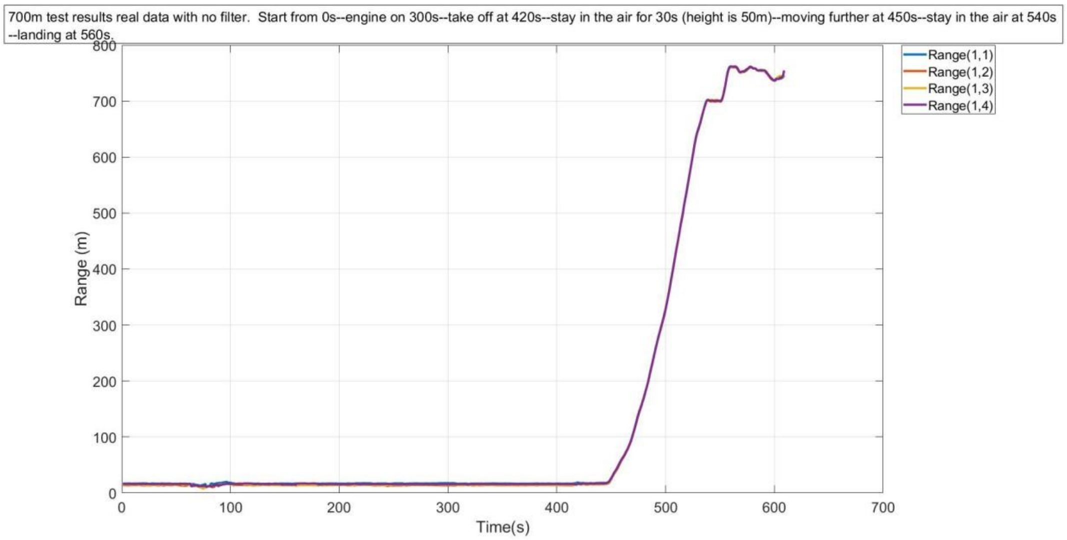

Figure 6.8: Range estimates for the short range test. The system maintained its ranging precision for the duration of the 750 m flight.

6.2.4 U-Turn Test

The fourth test followed the same flight path as the former, except that at the end of the runway we turned the drone around and returned it to the launch point. These results presented in Figure 6.9 are consistent with the previous test.

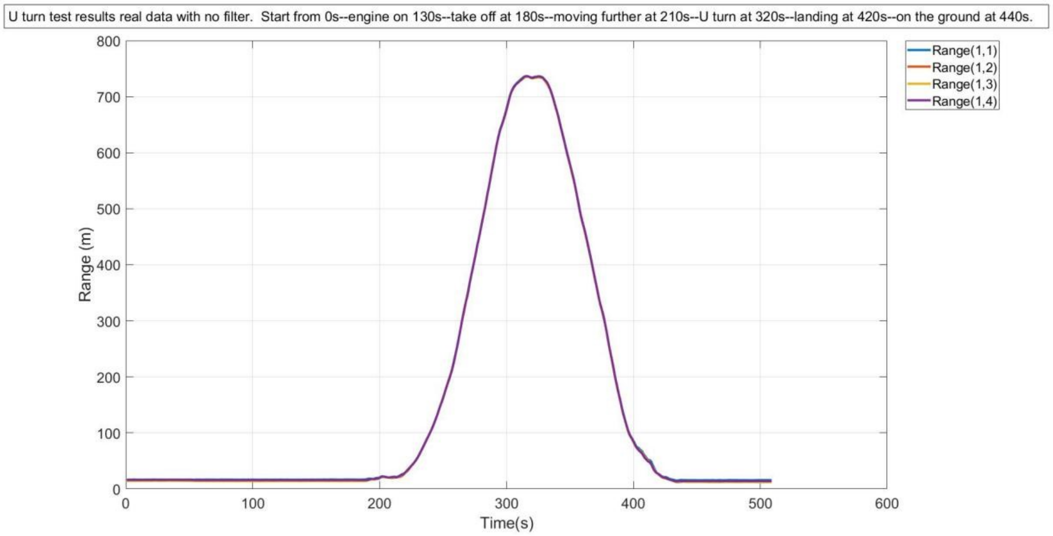

Figure 6.9: Range estimates for the U-turn test.

6.2.5 Long Range Test

The final test investigated the maximum range of the joint positioning-communications system. The drone was placed in a car and driven off site. The system maintained connection until the car reached the highway, at which point the signal was lost. We opened the trunk to restore the LOS between the drone and the base-station, and the system regained connection. After 2.6 km the system again lost connection.

Chapter 7

TECHNICAL CONSIDERATIONS

This chapter addresses some of the technical considerations made when designing and implementing the joint positioning-communications system. We discuss the communications link budget, co-channel interference, and a detailed examination of the ToA estimator performance.

7.1 Link Budget

The communications link budget is an expression of how much power is received of a transmission after accounting for physical and system losses. This budget is used to motivate decisions on parameter selection and waveform design. We compute a simple link budget for the system and select system parameters accordingly. Consider the simple line of sight channel attenuation

$$P_r = P_t \frac{G_{tx} G_{rx} \lambda^2}{(4\pi R)^2}. \tag{7.1}$$

Define the following parameters:

• P_t :	250mW
• G_{tx} :	0dB
• G_{rx} :	0dB
• λ(@750MHz) :	0.4m

The system specifications state that the system should remain operational at a range of up to 10 km, so we determine the link budget at that range:

$$P_r = 250(\text{mW}) \frac{1 \times 1 \times (0.4(\text{m}))^2}{(4\pi 10,000(\text{m}))^2} = -86 \text{ dBm}. \tag{7.2}$$

Consider a worst-case loss factor $L = 15$ dB such that the received SNR is

$$\text{SNR (dB)} = P_r - N - B - L \tag{7.3}$$

$$= -86 - (-174) - 70 - 15 \tag{7.4}$$

$$= 3 \text{ dB}, \tag{7.5}$$

where N is thermal noise at 1 Hz and B is the system bandwidth of 10 MHz. The capacity of this link is therefore

$$C = \log_2(1 + \text{SNR}) \tag{7.6}$$

$$= \log_2(1 + 2) \tag{7.7}$$

$$= 1.6 \text{ b/s/Hz}. \tag{7.8}$$

This is the maximum spectral efficiency that this link can support without loss. We must therefore choose system parameters that set the system's spectral efficiency below this maximum. This spectral efficiency is determined my the modulation order, code rate, and spread factor. Using MSK modulation, a rate 1/2 convolutional encoder, and a spread factor of 16, the actual system spectral efficiency is

$$\text{S.E.} = \text{bps} \times \text{rate} \times \text{spread}^{-1} \tag{7.9}$$

$$= 1 \times \frac{1}{2} \times \frac{1}{16} \tag{7.10}$$

$$= 0.03 \text{ b/s/Hz}. \tag{7.11}$$

This is well below the maximum capacity, so the link is well supported. This data rate may therefore be significantly increased in future iterations of the waveform design.

7.2 Co-Channel Interference

This system is susceptible to interference from nearby frequency allocations. We consider 2 primary sources of co-channel interference: spectral leakage of the neighbor into the operating band, and sidelobes of the pulse shaping filter. We assume that the former is sufficiently mitigated by the interferer's pulse shaping filter, and focus on the impact of spectral leakage as a result of pulse shaping side lobes.

Interferer spectral leakage will increase the amount of noise energy in the system and lower the signal to interference plus noise ratio (SINR). We evaluate the reduction in SINR for 2 potential interferers: one with 10 MHz bandwidth centered at a carrier frequency 20 MHz away from the center frequency, and one with 10 MHz bandwidth centered at 40 MHz away from the carrier frequency. We apply the pulse shaping filter and evaluate how much energy leaks into the signal. This is evaluated for 3 link ranges, for a total of 6 curves.

In Figure 7.1, the ratio of interference plus noise power to noise power is plotted as a function of the ratio of interference power to signal power. In Figure 7.2, the post-filter SINR is plotted as a function of the ratio of interference power to signal power. In Figure 7.3, the post-filter SINR is plotted against the pre-filter interference to noise ratio (INR).

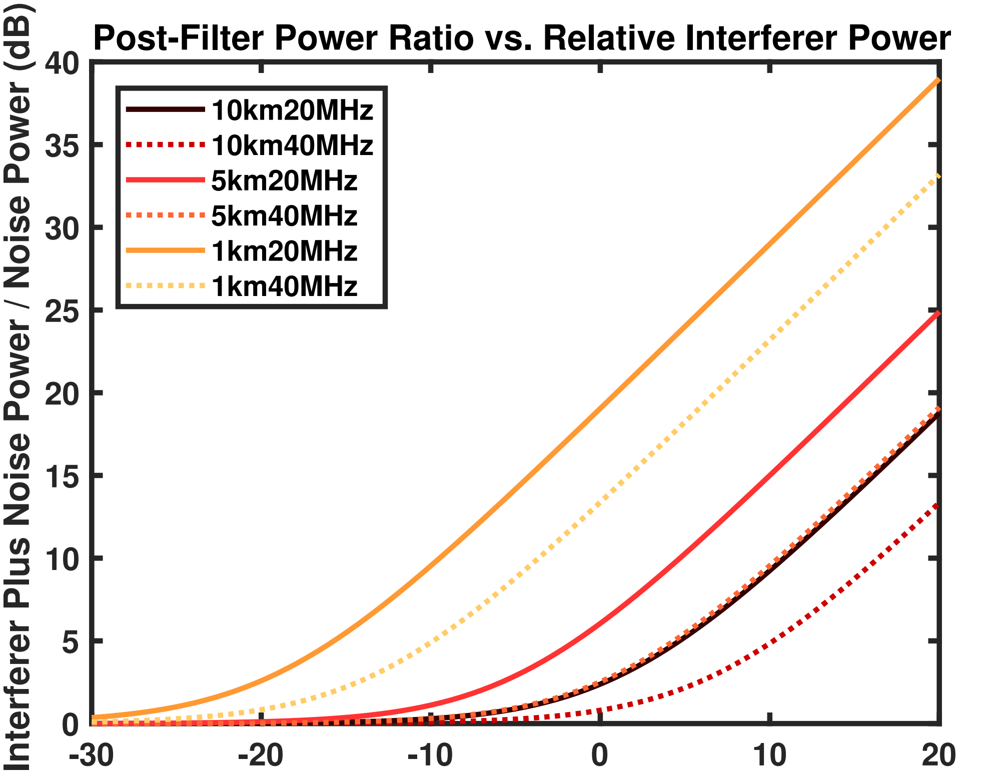

Figure 7.1: Interference plus noise / noise power vs interference / signal power. This depicts the effective increase in total noise power as a function of the ratio of received interferer power to received signal power.

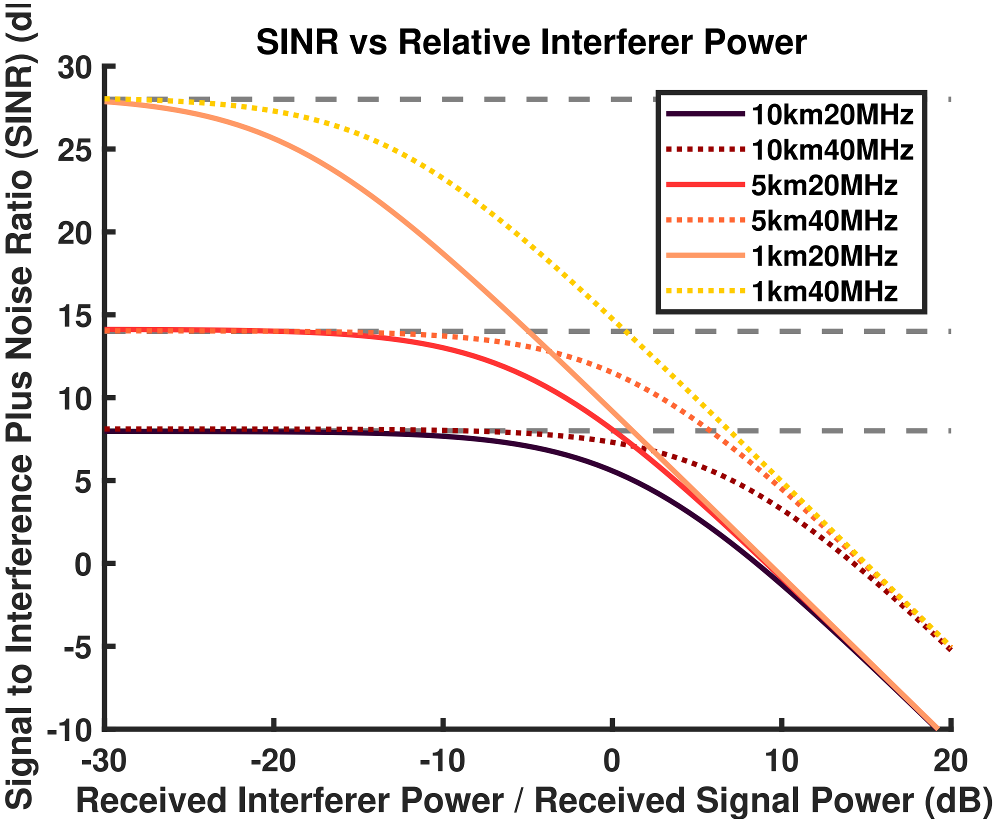

Figure 7.2: SINR vs interference / signal power. This depicts the effective decrease in SNR as a function of the ratio of received interferer power to received signal power. As the interferer power increases, the received noise is dominated by the interferer, which effectively becomes the noise floor. This creates the asymptotes above.

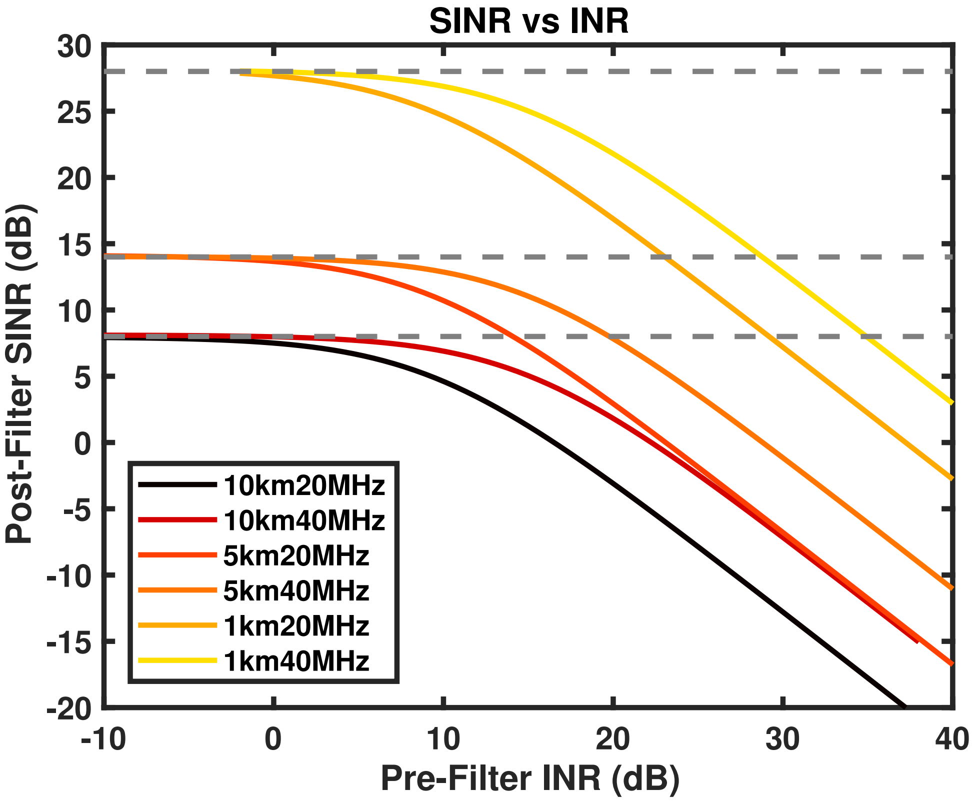

Figure 7.3: Post-filter SINR vs pre-filter INR. This characterizes the reduction in system SINR as a function of how powerful the interferer is compared to the noise floor. This is plotted for 3 link ranges for interferes 20 MHz and 40 MHz away, both operating with 10 MHz bandwidths.

7.3 Estimator Performance

We build a more comprehensive evaluation of the ToA estimator performance than the initial Cramer-Rao lower bound discussed in Chapter 3.

7.3.1 Probability of Cycle Errors

In the low SNR regime, the phase recovery estimator performance is dominated by cycle errors, which are caused by choosing one of the ambiguous phase solutions. This phenomenon is referred to as a cycle error or cycle slip. Cycle errors cause long tails in the distribution of errors, so the net variance of the estimator does not outperform the envelope recovery estimator until the probability of cycle error is driven to zero. The probability of cycle error for the phase recovery estimator is simulated in a Monte Carlo simulation environment as a function of the bandwidth to carrier ratio and the integrated SNR. The results are displayed in Figure 7.4.

7.3.2 Phase Compensation Error Distribution

The previous simulated result is extended by plotting histograms of the errors for a fixed ratio and a range of integrated SNRs. This reveals how often the nearby ambiguous solutions are chosen as a function of ISNR. This is depicted in Figure 7.5.

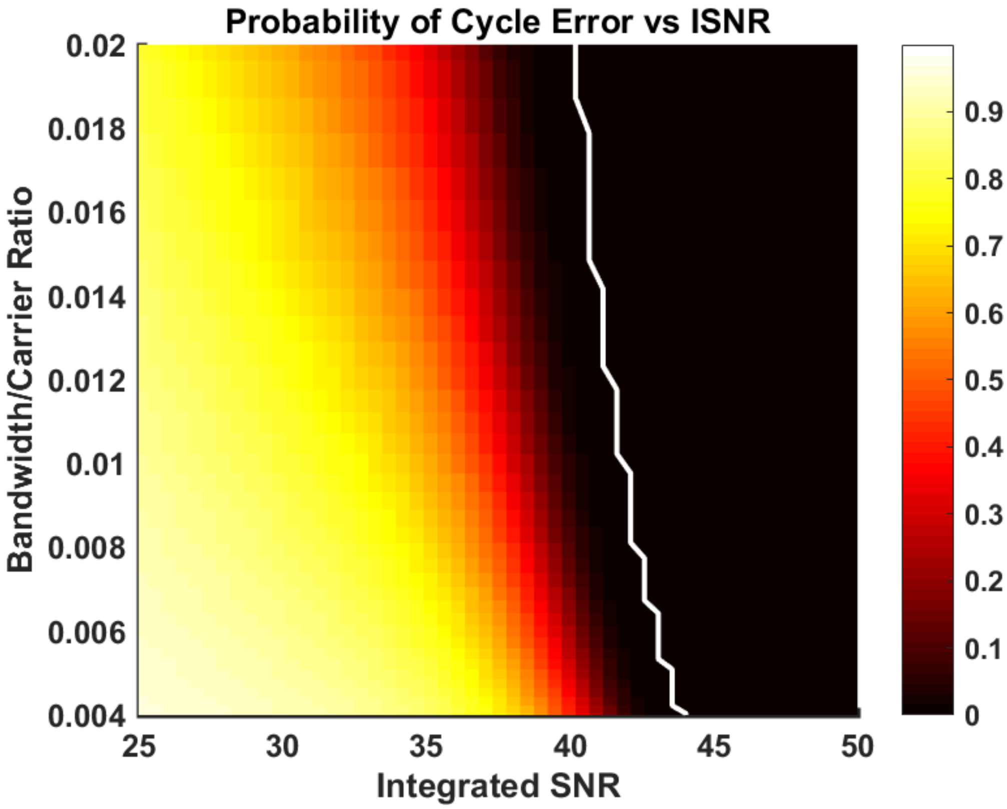

Figure 7.4: Probability of cycle error as a function of the bandwidth to carrier ratio and the integrated SNR. Higher SNR improves the estimator performance and reduces the likelihood of a cycle error. Increasing the bandwidth to carrier ratio decreases the number of cycles per sample, which reduces the number of potentially ambiguous solutions. The white line is the contour corresponding to a probability of 10^{-6}.

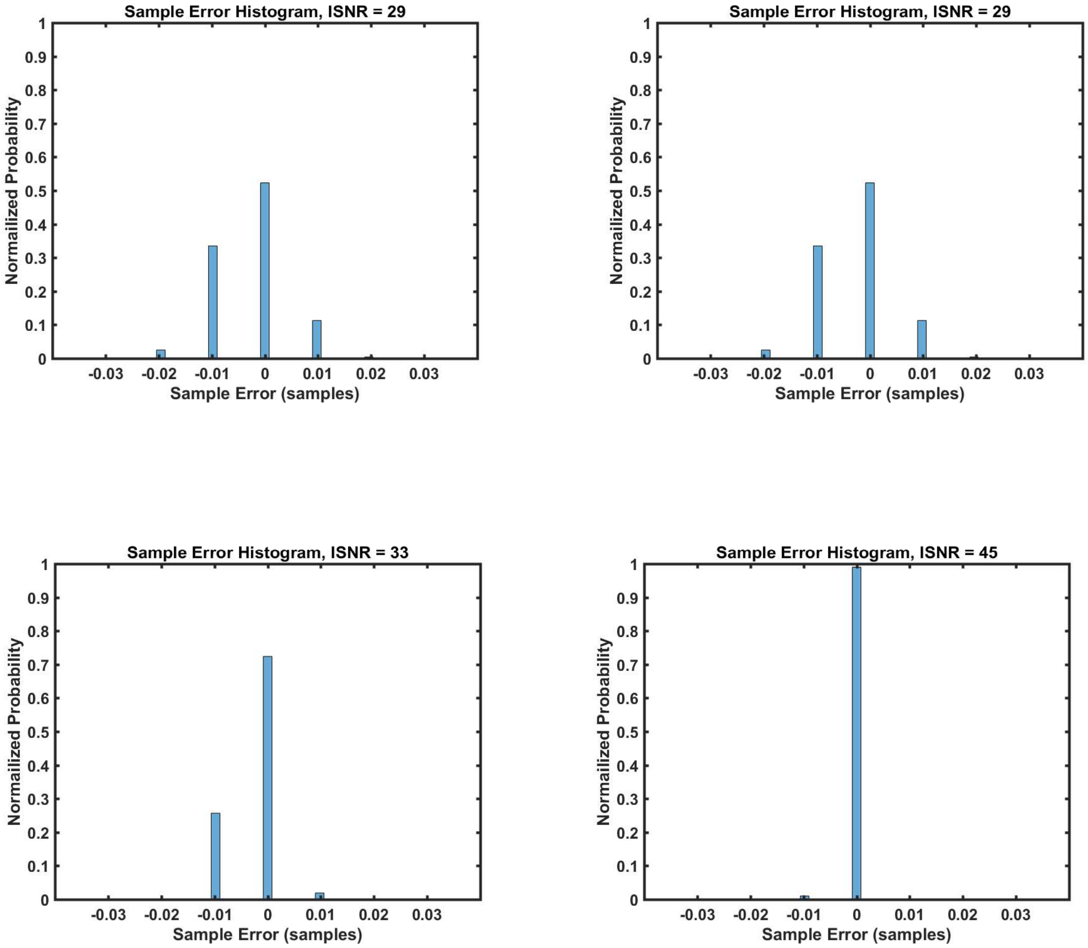

Figure 7.5: Error distribution of the phase recovery estimator at a fixed bandwidth to carrier ratio for a range of integrated SNRs. As the SNR increases, the likelihood of choosing the nearby ambiguities decreases, reducing the estimator variance. The threshold point for this probability being driven to 0 is consistent with previous results (∼45 dB).

7.4 Carrier Frequency Offset Estimation

Because phase is measured modulo 2π, the carrier frequency offset estimator cannot distinguish how many phase rotations occured between the two test points. This creates periodic ambiguities in the estimate, proportional to the inverse of the time between the test points. Consider the measured phases of the preamble and first postamble, ϕ_1 and ϕ_2, and the time difference between them, T_1. A coarse frequency estimate is

$$\hat{f}_1 = \frac{\hat{\phi}_2 - \hat{\phi}_1}{2\pi T_1}, \tag{7.12}$$

where $\hat{\phi}_1$ and $\hat{\phi}_2$ are the measured phases and $\hat{f}_1$ is the frequency offset estimate. This formulation assumes implicitly that less than one full rotation has occurred over the interval T. These phases are measured modulo 2π, so the phase ϕ_2 is indistinguishable from $\phi_2 \pm 2\pi n$, where n is any integer. This creates ambiguous solutions for $\hat{f}_1$ at $\pm n/T$.

If the clock sources are stable and well calibrated, the carrier frequency offset should be near zero. The expected range of this offset can be estimated given the clock specifications. The choice of T_1 will determine the locations of the ambiguities, so if T_1 is chosen such that the ambiguities lie outside of the expected range of frequency offsets, they can be safely ignored. By choosing small values of T_1, these ambiguities can be push arbitrarily far away. Unfortunately, small values of T_1 also increase the variance of the frequency estimate. The CRLB for frequency estimation of a sinusoid is [66]

$$\operatorname{var}(\hat{f}) \geq \frac{12\, f_s^2}{(2\pi)^2 \eta N(N^2-1)} \approx \frac{12}{(2\pi)^2} \frac{1}{\mathrm{ISNR}} \frac{1}{T^2}, \tag{7.13}$$

where η is the SNR, N is the length of the integration in samples, f_s is the sampling rate, and ISNR is the integrated SNR. In choosing T_1 we must therefore carefully consider both the ambiguities and the variance of the estimator.

To address both the ambiguities and the estimator performance, we use a two-stage estimator that first uses a small value of T to break the ambiguities, then uses a larger T to refine the variance of the estimate. The first estimate is the same as (7.12), with a choice of T_1 that places the ambiguities twice as far away as the maximum expected offset given the clock specifications. The second estimate is

$$\hat{f}_2 = \frac{\hat{\phi}_3 - \hat{\phi}_1 \pm 2\pi n}{2\pi T_2}, \; n = \arg\min(\hat{f}_2 - \hat{f}_1), \tag{7.14}$$

where ϕ_3 is the measured phase of the second postamble. This explicitly avoids the ambiguities by using the first estimate to choose the ambiguous solution closest to the original.

Clock sources with 100 ppb tolerance at 1 GHz should be accurate to within 100 Hz. For $T_1 = 0.84$ ms, the ambiguities occur at multiples of about 1.7 kHz, so the estimator can easily disambiguate the solutions for sufficient SNR. At 3 dB instantaneous SNR, this estimator achieves a standard deviation of about 11 Hz. The second stage uses $T_2 = 1.26$ ms, which achieves a lower standard deviation of 7 Hz. Both choices are conservative: T_1 is much larger than it needs to be to guarantee that the ambiguities do not affect the estimate, and T_2 is shorter than it could be given that the first estimate breaks the ambiguities. In future iterations of the waveform design, these parameters can be safely tuned to improve the estimator performance.

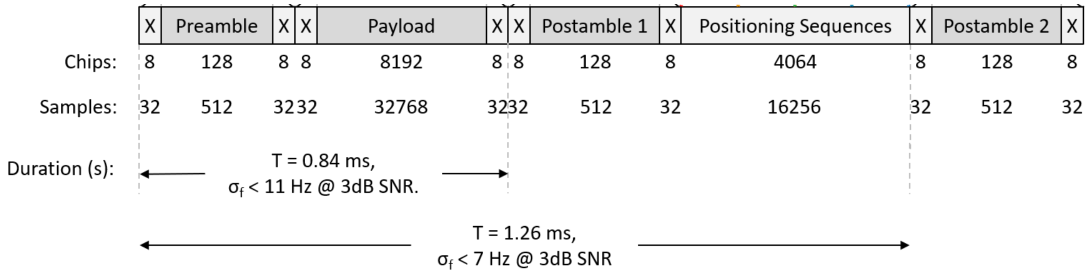

	X	Preamble	X	X	Payload	X	X	Postamble 1	X	Positioning Sequences	X	Postamble 2	X
Chips:	8	128	8	8	8192	8	8	128	8	4064	8	128	8
Samples:	32	512	32	32	32768	32	32	512	32	16256	32	512	32

Figure 7.6: Depiction of two frequency estimators using the preamble and postambles. The first estimator easily disambiguates the estimate but has a worse estimate. The second estimator has a better estimate but is susceptible to the ambiguities. The first estimate is used to disambiguate the second estimator. The reported standard deviations represent the worst-case scenario at 10 km given the system parameters and link budget (which result in 3 dB SNR).

7.5 LTE Integration

In this section, I discuss integration of the joint positioning-communications (JPC) system into existing Long-Term Evolution (LTE) cellular networks. Exploiting the existing LTE infrastructure requires a new waveform design that is compatible with the LTE standard, and a new data link layer that cooperates with LTE resource allocation and user scheduling protocols. Integration with LTE requires a redesign of the physical and data link layers.

Long-Term Evolution (LTE) is a standard for wireless broadband communications, primarily used for mobile devices and data terminals. This standard supports high-speed wireless data networks using an Orthogonal Frequency-Division Multiplexing (OFDM) waveform, adjustable carrier bandwidths, and frequency division duplexing (FDD) or time division duplexing (TDD) modes. LTE offers significant flexibility in terms of modulation schemes, carrier bandwidth, resource allocation, and user scheduling, making it an excellent candidate for integration with the proposed technology. LTE cellular networks already have extensive infrastructure and coverage in many countries, which could enable immediate integration of joint positioning-communications networking applications to numerous users [67].

7.5.1 LTE Integration: Physical Layer

The physical layer is the 1st layer in the OSI model. This layer defines how data is physically passed between nodes in a network. LTE already has a physical layer definition, so the JPC system must be modified to fit within the LTE protocol definitions. The JPC waveform was originally designed to accommodate a specifically-sized payload. To integrate this payload into LTE waveforms, the size must be adjusted and the payload must be split into multiple slots.

The current communications payload is 8192 chips long. Each LTE slot contains 7 OFDM symbols, each of which has a useful symbol length of 2048 chips. The integrated payload must therefore be divided into at least 4 OFDM symbols. Depending on further additions to the content of the payload, and to facilitate the receiver parsing the received LTE frames, it may be beneficial to expand the payload to cover all 7 OFDM symbols in a given slot. This would allow a payload length of 14336 chips, a 75% increase over the original waveform, and simplifies the receive chain processing [68].

The positioning sequences are independent sequences that are treated to have low cross-correlations with each other. They do not necessarily need to be transmitted in sequence, as in Figure 2.3, as long as the transmit times are recorded and shared. The standard OFDM symbols in an LTE slot are 2192 chips long, which are already 119% longer than the current JPC definition, thus a single OFDM symbol should be sufficient for each positioning sequence. There are only 7 symbols in an LTE slot, however, and given that the payload must occupy at least 4 of the symbols, we cannot fit all of the payload and all of the positioning sequences in a single slot. We therefore assume that a transmission must occupy at least 2 slots, preferably adjacent. If the JPC system is to be modified to fit 2 slots (14 OFDM symbols), then the LTE integration can support the following configurations:

1. **Payload: 4 symbols, Positioning: 4 symbols, Extra: 6 symbols.**

   This configuration most closely matches the current JPC waveform design, with a slightly large payload and doubly long positioning sequences. There are 6 extra symbols during which additional information can be added, such as pre- and post-ambles or additional positioning sequences to support more antennas.

2. **Payload: 7 symbols, Positioning: 4 symbols, Extra: 3 symbols.**

   This configuration expands the communications payload to accommodate more data as discussed above. This still leaves enough room for 4 positioning sequences and 3 reserved symbols for ambles or more antennas.

If the uplink can reserve two adjacent slots for the transmission of the payload and positioning sequences, the system has flexibility in terms of placing and ordering the transmit waveforms. Given the configurations listed above, reordering certain OFDM symbols may help mitigate multi-path, inter-symbol interference, and time-frequency channel fading, as well as improve frequency offset estimates [69].

7.5.2 LTE Integration: Data Link Layer

In this section, we discuss potential changes to the JPC data link layer that enable compatibility with the LTE data link layer (DLL). The legacy JPC system is only defined as a point-to-point positioning-communications system, so it lacks a protocol for distributing spectral and temporal access for large networks of users. The LTE standard defines how uplink and downlink transmissions are scheduled, and how different users are granted access to time-frequency resource elements. An integrated LTE JPC data link layer must address the following concerns in this regard:

- **Time Slots:** As discussed in the previous section, a JPC user needs two consecutive slots (2x 0.5 ms) to complete a transmission. We assume that all

JPC traffic is considered uplink traffic by the LTE network, and as such the integrated DLL must schedule uplink/downlink according to this constraint.

- **Frequency Slots:** The JPC receiver is sensitive to interference from nearby frequency bands. It is likely that nearby users operating in adjacent frequency allocations will interfer with each other, so the DLL must distribute JPC traffic to avoid co-channel interference.

- **Traffic Dependent Scheduling:** Depending on the volume of JPC traffic, the DLL may decide to allow a user to transmit over more than one frequency bin to increase throughput and positioning performance. A protocol must be designed that identifies the available resources and appropriately allocate them.

- **Channel Dependent Scheduling:** Because LTE operates over such a large frequency range, it is possible that some users may experience significantly greater fading in some frequency bins than others. If the network traffic is sufficiently low, it is possible to adaptively reallocate frequency slots to different users to maximize overall performance.

7.5.3 Frequency Offset Estimation

The current JPC system estimates frequency offsets by placing a pre-amble and post-amble around the communications payload, and a second postamble after the positioning sequences. Both configurations above allow for these three sequences to be added at arbitrary locations, which may improve the frequency offset estimation by providing longer sequences to correlate and a large separation to reduce the estimator variance.

An alternative to using the legacy dual-pilot technique is to use the cyclic prefix of the OFDM symbols to perform the carrier frequency offset (CFO) estimation [70, 71].

Depending on the necessary precision, this may be sufficient for estimating the offset without the need for any additional pilot sequences, which allows the extra symbols to support increased data throughput or additional platform antennas. Two estimators are proposed in [70, 71] for carrier frequency offset (CFO) estimation. We evaluate the performance of each estimator based on their respective Cramèr Rao Lower Bounds (CRLBs) for example parameter values.

7.5.4 Legacy Integrated Estimation

The first estimator uses two pilot sequences of N chips separated by T seconds. The estimator estimates the phase of each pilot sequence, then divides the difference by $2\pi T$ to estimate the CFO in Hz. For pilot sequences of the same length, and reasonably large N, the CRLB for this estimator is [70]

$$\sigma_f^2 \geq \frac{8}{(2\pi)^2 T^2 N \eta}, \tag{7.15}$$

where η is the SNR of the received sequences. This estimator suffers from ambiguities at $\pm n/T$ Hz, $n \in [1, 2, ...]$, because it cannot tell how many rotations have occurred between the two pilot sequences. This is addressed in the legacy JPC system by placing two pilot sequences very close together, which makes the ambiguities very well separated, then assuming that the smallest solution is the correct estimate. This solution is then used to disambiguate a second estimator with a third, much further separated pilot sequence.

If this estimator were to be integrated into the LTE physical layer discussed earlier, a reasonable waveform configuration would be

1x Pilot / 1x Payload (1/7) / 1x Pilot / 6x Payload (6/7) / 4x Nav / 1x Pilot

In this configuration, the distance between near pilots is $T_1 = 71.3$ μs, and the distance between the far pilots is $T_2 = 926.9$ μs. The ambiguities are 14.0 kHz and 1.08 kHz respectively. Based on the hardware specifications, it is safe to assume that the carrier offset is significantly less than 1 kHz, so there is no need to disambiguate the estimate. The resulting performance bound is therefore

$$\sigma_f \geq \sqrt{\frac{8}{(2\pi)^2(926.9 \times 10^{-6})^2(2192)(2)}} = 7.33 \text{ Hz}, \tag{7.16}$$

where 2192 is the length of an OFDM symbol in chips and $\eta = 2$ is chosen to be consistent with the calculations in Figure 2.3.

7.5.5 Cyclic Prefix Estimation

Instead of relying on the legacy CFO estimation technique, we may leverage the cyclic prefixes already present in the OFDM symbols to implement the estimator. A CFO estimation algorithm is outlined in [71] and the CRLB is derived as

$$\sigma_f^2 \geq \frac{(1-\rho^2)}{8\pi^2\rho^2 L}, \tag{7.17}$$

where $\rho = \text{SNR} \;/\; (\text{SNR} + 1)$ and L is the length of the CP in chips. Using the same parameters as above, the performance of this estimator is

$$\sigma_f \geq \sqrt{\frac{(1-(2/3)^2)}{8\pi^2(2/3)^2(144/10^7)}} = 10.49 \text{ Hz}, \tag{7.18}$$

where $144/10^7$ is the length of the CP in seconds at 10 MHz bandwidth. This estimator demonstrates comparable performance to the legacy estimator in the best case scenario, indicating that the pilot sequences cna be excluded in favor a CP-based CFO estimation algorithm, which in turn increases the system's flexibility in terms of throughput and platform antennas.

Chapter 8

SUMMARY AND FUTURE WORK

8.1 Summary

Modern vehicle systems demand increasingly sophisticated positioning technologies in increasingly cluttered environments. Legacy radio systems do not support modern performance requirements or user densities. We designed and implemented a joint positioning-communications system as a next-generation positioning technology that promises a low-cost, high-performance solution to this problem. This technology offers extreme ranging precision (< 5 cm) with minimal bandwidth (10 MHz), a secure communications link to protect against cyberattacks, a small form factor that enables integration into numerous platforms, and minimal resource consumption which supports high-density networks. This system operates with minimal infrastructure and is highly re-configurable to execute a variety of missions.

This system is a joint positioning-communications radio technology that simultaneously performs relative positioning and secure communications. Both tasks are performed simultaneously with a single, co-use waveform, which efficiently utilizes limited resources and supports higher user densities. The positioning tasks uses a cooperative, point-to-point synchronization protocol to estimate the relative position and orientation of all users within the network. This technology may be installed in ground-stations, ground vehicles, unmanned aerial systems, and airborne vehicles, enabling a highly-mobile, re-configurable network. The communications task distributes positioning information between users and secures the positioning task against cyberattacks.

This technology has numerous applications to modern vehicle systems. High-precision relative positioning enables applications such as collision avoidance, automated landing, navigation, and formation control. Secure network communications enable distributed knowledge base, real-time traffic conditions, and air traffic management, and when combined with the positioning task maintains distributed coherence between users. The system flexibility allows quick and easy installation in areas without existing coverage, providing immediate support in situations such as disaster relief or forward operating bases. This technology further supports automation of vehicular transport by providing a cooperative medium between users, enabling vehicle-to-vehicle communications and remote control.

8.2 Future Work

The joint positioning-communications system is still being actively developed by the research group and is constantly evolving to incorporate new capabilities, adapting to new applications, and becoming more robust to real-world limitations. We are currently investigating the following issues:

- Implementing phase reset and phase refinement estimators on experimental hardware testbeds. The current hardware and phase reset techniques lack the fidelity to achieve the desired sub-centimeter precision. We are currently investigating methods to improve the phase reset on the hardware, as well as considering an integrated approach where the phase information is instead used by the synchronization algorithm to jointly estimate the state space parameters and the phase correctiosn to the ToA.

- Exploring lower bounds on position and orientation estimators given the ToA and ToF estimation techniques. The fidelity of position and orientation estimators are affected not only by the precision of the ToA estimates, but also by the distribution of antennas on the platform. This effect is commonly referred to as geometric dilution of precision (GDOP). We have developed closed-form lower bounds on 3-D position estimates that incorporate both the CRLB on ToA and the effects of GDOP. We are working on building a set of Monte-Carlo simulations that verify these lower bounds for multiple antenna configurations.

- Exploring a network extension of the system architecture to include larger networks of users, possibly as an integration with existing infrastructure such as LTE systems. The JPC system currently lacks a comprehensive network layer to handle multiple users in dynamic network environments. We are developing a suite of network protocols to enable more comprehensive network applications, as well as considering modifications to the system to allow integration into existing networks, such as LTE.

REFERENCES

[1] P. Bidigare, U. Madhow, R. Mudumbai, and D. Scherber, “Attaining fundamental bounds on timing synchronization,” in *Acoustics, Speech and Signal Processing (ICASSP), 2012 IEEE International Conference on.* IEEE, 2012, pp. 5229–5232.

[2] P. Bidigare, S. Pruessing, D. Raeman, D. Scherber, U. Madhow, and R. Mudumbai, “Initial over-the-air performance assessment of ranging and clock synchronization using radio frequency signal exchange,” in *Statistical Signal Processing Workshop (SSP), 2012 IEEE.* IEEE, 2012, pp. 273–276.

[3] B. Paul, A. R. Chiriyath, and D. W. Bliss, “Survey of rf communications and sensing convergence research,” *IEEE Access*, vol. 5, pp. 252–270, 2017.

[4] J. Harding, G. Powell, R. Yoon, J. Fikentscher, C. Doyle, D. Sade, M. Lukuc, J. Simons, J. Wang *et al.*, “Vehicle-to-vehicle communications: readiness of v2v technology for application.” United States. National Highway Traffic Safety Administration, Tech. Rep., 2014.

[5] A. Cailean, B. Cagneau, L. Chassagne, S. Topsu, Y. Alayli, and J.-M. Blosseville, “Visible light communications: Application to cooperation between vehicles and road infrastructures,” in *Intelligent Vehicles Symposium (IV), 2012 IEEE.* IEEE, 2012, pp. 1055–1059.

[6] P. Lowbridge, “Low cost millimeter-wave radar systems for intelligent vehicle cruise control applications,” *Microwave Journal*, vol. 38, no. 10, pp. 20–27, 1995.

[7] J. Michael, “Phased array based radar system for vehicular collision avoidance,” Nov. 14 1995, U.S. Patent 5,467,072.

[8] Y. K. Kwag and C. H. Chung, “Uav based collision avoidance radar sensor,” in *2007 IEEE International Geoscience and Remote Sensing Symposium.* IEEE, 2007, pp. 639–642.

[9] R. A. LeMire and J. M. Branning Jr, “Systems and methods for collision avoidance in unmanned aerial vehicles,” Feb. 19 2013, U.S. Patent 8,378,881.

[10] A. Sarkar, S. Agarwal, and A. Nath, “Li-fi technology: Data transmission through visible light,” *International Journal of Advance Research in Computer Science and Management Studies*, vol. 3, no. 6, 2015.

[11] S. Preethi, “Collision avoidance using li-fi based inter vehicle communication,” *Journal of Network Security*, vol. 6, no. 2, pp. 22–26, 2018.

[12] R. Sabatini, A. Gardi, and M. Richardson, “Lidar obstacle warning and avoidance system for unmanned aircraft,” *International Journal of Mechanical, Aerospace, Industrial and Mechatronics Engineering*, vol. 8, no. 4, pp. 718–729, 2014.

[13] A. Mukhtar, L. Xia, and T. B. Tang, “Vehicle detection techniques for collision avoidance systems: A review,” *IEEE Transactions on Intelligent Transportation Systems*, vol. 16, no. 5, pp. 2318–2338, 2015.

[14] D. C. Shaw and J. Z. Shaw, “Vehicle collision avoidance system,” Jun. 25 1996, U.S. Patent 5,529,138.

[15] V. A. Orlando, “The mode s beacon radar system,” *The Lincoln Laboratory Journal*, vol. 2, no. 3, pp. 345–362, 1989.

[16] M. Strohmeier, M. Schafer, V. Lenders, and I. Martinovic, “Realities and challenges of nextgen air traffic management: the case of ads-b,” *IEEE Communications Magazine*, vol. 52, no. 5, pp. 111–118, 2014.

[17] O. A. Yeste-Ojeda, J. Zambrano, and R. Landry, “Design of integrated mode s transponder, ads-b and distance measuring equipment transceivers,” in *Integrated Communications Navigation and Surveillance (ICNS), 2016*. IEEE, 2016, pp. 4E1–1.

[18] N. Decarli, F. Guidi, and D. Dardari, “A novel joint rfid and radar sensor network for passive localization: Design and performance bounds,” *IEEE Journal of Selected Topics in Signal Processing*, vol. 8, no. 1, pp. 80–95, 2014.

[19] P. Bidigare, “The shannon channel capacity of a radar system,” in *Signals, Systems and Computers, 2002. Conference Record of the Thirty-Sixth Asilomar Conference on*, vol. 1. IEEE, 2002, pp. 113–117.

[20] X. Shaojian, C. Bing, and Z. Ping, “Radar-communication integration based on dsss techniques,” in *Signal Processing, 2006 8th International Conference on*, vol. 4. IEEE, 2006.

[21] M. Jamil, H.-J. Zepernick, and M. I. Pettersson, “On integrated radar and communication systems using oppermann sequences,” in *Military Communications Conference, 2008. MILCOM 2008. IEEE*. IEEE, 2008, pp. 1–6.

[22] X. Li, R. Yang, Z. Zhang, and W. Cheng, “Research of constructing method of complete complementary sequence in integrated radar and communication,” in *Signal Processing (ICSP), 2012 IEEE 11th International Conference on*, vol. 3. IEEE, 2012, pp. 1729–1732.

[23] C. Sturm, T. Zwick, and W. Wiesbeck, “An ofdm system concept for joint radar and communications operations,” in *Vehicular Technology Conference, 2009. VTC Spring 2009. IEEE 69th*. IEEE, 2009, pp. 1–5.

[24] D. Garmatyuk, J. Schuerger, Y. Morton, K. Binns, M. Durbin, and J. Kimani, “Feasibility study of a multi-carrier dual-use imaging radar and communication system,” in *Radar Conference, 2007. EuRAD 2007. European*. IEEE, 2007, pp. 194–197.

[25] G. Wunder and H. Boche, "Upper bounds on the statistical distribution of the crest-factor in ofdm transmission," *IEEE Transactions on Information Theory*, vol. 49, no. 2, pp. 488–494, 2003.

[26] S. C. Thompson and J. P. Stralka, "Constant envelope ofdm for power-efficient radar and data communications," in *Waveform Diversity and Design Conference, 2009 International.* IEEE, 2009, pp. 291–295.

[27] S. Gogineni, M. Rangaswamy, and A. Nehorai, "Multi-modal ofdm waveform design," in *Radar Conference (RADAR), 2013 IEEE.* IEEE, 2013, pp. 1–5.

[28] M. Kiviranta, A. Mammela, D. Cabric, D. A. Sobel, and R. W. Brodersen, "Constant envelope multicarrier modulation: performance evaluation awgn and fading channels," in *Military Communications Conference, 2005. MILCOM 2005. IEEE.* IEEE, 2005, pp. 807–813.

[29] A. U. Ahmed, S. C. Thompson, and J. R. Zeidler, "Channel estimation and equalization for ce-ofdm in multipath fading channels," in *Military Communications Conference, 2008. MILCOM 2008. IEEE.* IEEE, 2008, pp. 1–7.

[30] B. Donnet and I. Longstaff, "Combining mimo radar with ofdm communications," in *Radar Conference, 2006. EuRAD 2006. 3rd European.* IEEE, 2006, pp. 37–40.

[31] M. Braun, C. Sturm, A. Niethammer, and F. K. Jondral, "Parametrization of joint ofdm-based radar and communication systems for vehicular applications," in *Personal, Indoor and Mobile Radio Communications, 2009 IEEE 20th International Symposium on.* IEEE, 2009, pp. 3020–3024.

[32] Y. Xie, R. Tao, and T. Wang, "Method of waveform design for radar and communication integrated system based on css," in *Instrumentation, Measurement, Computer, Communication and Control, 2011 First International Conference on.* IEEE, 2011, pp. 737–739.

[33] X. Chen, X. Wang, S. Xu, and J. Zhang, "A novel radar waveform compatible with communication," in *Computational Problem-Solving (ICCP), 2011 International Conference on.* IEEE, 2011, pp. 177–181.

[34] G. N. Saddik, R. S. Singh, and E. R. Brown, "Ultra-wideband multifunctional communications/radar system," *IEEE Transactions on Microwave Theory and Techniques*, vol. 55, no. 7, pp. 1431–1437, 2007.

[35] A. Springer, W. Gugler, M. Huemer, L. Reindl, C. Ruppel, and R. Weigel, "Spread spectrum communications using chirp signals," in *EUROCOMM 2000. Information Systems for Enhanced Public Safety and Security. IEEE/AFCEA.* IEEE, 2000, pp. 166–170.

[36] S. D. Blunt, M. Cook, J. Jakabosky, J. De Graaf, and E. Perrins, "Polyphase-coded fm (pcfm) radar waveforms, part i: implementation," *IEEE Transactions on Aerospace and Electronic Systems*, vol. 50, no. 3, pp. 2218–2229, 2014.

[37] S. D. Blunt, J. Jakabosky, M. Cook, J. Stiles, S. Seguin, and E. Mokole, "Polyphase-coded fm (pcfm) radar waveforms, part ii: optimization," *IEEE Transactions on Aerospace and Electronic Systems*, vol. 50, no. 3, pp. 2230–2241, 2014.

[38] C. Sahin, J. Jakabosky, P. M. McCormick, J. G. Metcalf, and S. D. Blunt, "A novel approach for embedding communication symbols into physical radar waveforms," in *Radar Conference (RadarConf), 2017 IEEE*. IEEE, 2017, pp. 1498–1503.

[39] C. A. Mohr, P. M. McCormick, S. D. Blunt, and C. Mott, "Spectrally-efficient fm noise radar waveforms optimized in the logarithmic domain," in *Radar Conference (RadarConf18), 2018 IEEE*. IEEE, 2018, pp. 0839–0844.

[40] T. E. McEwan, "Time-of-flight radio location system," Apr. 23 1996, U.S. Patent 5,510,800.

[41] L. W. Fullerton, J. L. Richards, and I. A. Cowie, "System and method for position determination by impulse radio using round trip time-of-flight," Aug. 26 2003, U.S. Patent 6,611,234.

[42] S. Lanzisera, D. Zats, and K. S. Pister, "Radio frequency time-of-flight distance measurement for low-cost wireless sensor localization," *IEEE Sensors Journal*, vol. 11, no. 3, pp. 837–845, 2011.

[43] B. Hofmann-Wellenhof, H. Lichtenegger, and J. Collins, *Global positioning system: theory and practice*. Springer Science & Business Media, 2012.

[44] "Gps.gov: Program funding," https://www.gps.gov/policy/funding/, accessed: 2019-10-14.

[45] N. O. Tippenhauer, C. Pöpper, K. B. Rasmussen, and S. Capkun, "On the requirements for successful gps spoofing attacks," in *Proceedings of the 18th ACM conference on Computer and communications security*. ACM, 2011, pp. 75–86.

[46] D. L. Mills, "Internet time synchronization: the network time protocol," *IEEE Transactions on communications*, vol. 39, no. 10, pp. 1482–1493, 1991.

[47] D. Mills, "Network time protocol (version 3) specification, implementation and analysis," 1992.

[48] B. Sundararaman, U. Buy, and A. D. Kshemkalyani, "Clock synchronization for wireless sensor networks: a survey," *Ad hoc networks*, vol. 3, no. 3, pp. 281–323, 2005.

[49] S. Han, Z. Gong, W. Meng, C. Li, and X. Gu, "Future alternative positioning, navigation, and timing techniques: a survey," *IEEE wireless communications*, vol. 23, no. 6, pp. 154–160, 2016.

[50] S. Lo, Y. H. Chen, P. Enge, B. Peterson, R. Erikson, and R. Lilley, "Distance measuring equipment accuracy performance today and for future alternative position navigation and timing (apnt)," in *Proceedings of the 26th International Technical Meeting of The Satellite Division of the Institute of Navigation (ION GNSS 2013), Nashville, TN*, 2013, pp. 711–721.

[51] K. Pourvoyeur, A. Mathias, and R. Heidger, "Investigation of measurement characteristics of mlat/wam and ads-b," in *2011 Tyrrhenian International Workshop on Digital Communications-Enhanced Surveillance of Aircraft and Vehicles.* IEEE, 2011, pp. 203–206.

[52] M. A. Garcia, R. Mueller, E. Innis, and B. Veytsman, "An enhanced altitude correction technique for improvement of wam position accuracy," in *2012 Integrated Communications, Navigation and Surveillance Conference.* IEEE, 2012, pp. A4–1.

[53] H. Neufeldt and S. Stanzel, "An operational wam in frankfurt airspace," in *2013 14th International Radar Symposium (IRS)*, vol. 2. IEEE, 2013, pp. 561–566.

[54] S.-S. Jan, S. L. Jheng, Y. H. Chen, and S. Lo, "Evaluation of positioning algorithms for wide area multilateration based alternative positioning navigation and timing (apnt) using 1090 mhz ads-b signals," in *27th International Technical Meeting of the Satellite Division of the Institute of Navigation, ION GNSS 2014.* Institute of Navigation, 2014, pp. 3016–3028.

[55] "ADS-B frequently asked questions (faqs)," https://www.faa.gov/nextgen/programs/adsb/faq/#i2, accessed: 2010-10-17.

[56] J. Barnes, J. Wang, C. Rizos, and T. Tsujii, "The performance of a pseudolite-based positioning system for deformation monitoring," in *2nd Symp. on Geodesy for Geotechnical & Structural Applications*, 2002, pp. 21–24.

[57] D. Shutin, N. Schneckenburger, M. Walter, and M. Schnell, "Ldacs1 ranging performance-an analysis of flight measurement results," in *2013 IEEE/AIAA 32nd Digital Avionics Systems Conference (DASC).* IEEE, 2013, pp. 3C6–1.

[58] S. Tsugawa and S. Kato, "Energy its: another application of vehicular communications," *IEEE Communications Magazine*, vol. 48, no. 11, 2010.

[59] S. Eckelmann, T. Trautmann, H. Ußler, B. Reichelt, and O. Michler, "V2v-communication, lidar system and positioning sensors for future fusion algorithms in connected vehicles," *Transportation Research Procedia*, vol. 27, pp. 69–76, 2017.

[60] K.-D. Langer and J. Grubor, "Recent developments in optical wireless communications using infrared and visible light," in *Transparent Optical Networks, 2007. ICTON'07. 9th International Conference on*, vol. 3. IEEE, 2007, pp. 146–151.

[61] A. Belle, M. Falcitelli, M. Petracca, and P. Pagano, "Development of ieee802. 15.7 based its services using low cost embedded systems," in *ITS Telecommunications (ITST), 2013 13th International Conference on.* IEEE, 2013, pp. 419–425.

[62] B. W. Parkinson, P. Enge, P. Axelrad, and J. J. Spilker Jr, *Global positioning system: Theory and applications, Volume II.* American Institute of Aeronautics and Astronautics, 1996.

[63] P. Misra and P. Enge, "Global positioning system: signals, measurements and performance second edition," *Massachusetts: Ganga-Jamuna Press*, 2006.

[64] H. Zimmermann, "Osi reference model-the iso model of architecture for open systems interconnection," *IEEE Transactions on communications*, vol. 28, no. 4, pp. 425–432, 1980.

[65] C. A. Balanis, *Antenna theory: analysis and design.* John Wiley & Sons, 2016.

[66] S. M. Kay, "Fundamentals of statistical signal processing, volume i: Estimation theory (v. 1)," *PTR Prentice-Hall, Englewood Cliffs*, 1993.

[67] "Lte (telecommunication)," 2019, [Online; accessed 05-July-2019]. [Online]. Available: https://en.wikipedia.org/wiki/LTE_(telecommunication)

[68] A. Lucent, "The lte network architecture—a comprehensive tutorial," *Strategic Whitepaper*, 2009.

[69] R. D. Trivedi and M. C. Patel, "Comparison of different scheduling algorithm for lte," *International Journal of Emerging Technology and Advanced Engineering*, vol. 4, no. 5, pp. 334–339, 2014.

[70] J.-H. Yu and Y. T. Su, "Pilot-assisted maximum-likelihood frequency-offset estimation for ofdm systems," *IEEE Transactions on Communications*, vol. 52, no. 11, pp. 1997–2008, 2004.

[71] C. Athaudage and K. Sathananthan, "Cramer-rao lower bound on frequency offset estimation error in ofdm systems with timing error feedback compensation," in *2005 5th International Conference on Information Communications & Signal Processing.* IEEE, 2005, pp. 1231–1235.